JGR Atmospheres

RESEARCH ARTICLE
10.1029/2022JD036860

Ice Aggregation in Low-Level Mixed-Phase Clouds at a High Arctic Site: Enhanced by Dendritic Growth and Absent Close to the Melting Level

Giovanni Chellini[1], Rosa Gierens[1], and Stefan Kneifel[1,2]

[1]Institute for Geophysics and Meteorology, University of Cologne, Cologne, Germany, [2]Meteorological Institute, Ludwig-Maximilians-University Munich, Munich, Germany

Key Points:

- Low-level mixed-phase clouds (MPCs) at Ny-Ålesund produce large aggregates predominantly at dendritic-growth temperatures
- Enhanced aggregation due to dendritic growth occurs intermittently in limited regions of the MPC
- The typically observed enhanced aggregation zone close to 0°C is absent in low-level MPCs at the site

Correspondence to:
G. Chellini,
g.chellini@uni-koeln.de

Citation:
Chellini, G., Gierens, R., & Kneifel, S. (2022). Ice aggregation in low-level mixed-phase clouds at a high Arctic site: Enhanced by dendritic growth and absent close to the melting level. *Journal of Geophysical Research: Atmospheres*, *127*, e2022JD036860. https://doi.org/10.1029/2022JD036860

Received 1 APR 2022
Accepted 30 JUL 2022

Abstract Low-level mixed-phase clouds (MPCs) occur extensively in the Arctic, and are known to play a key role for the energy budget. While their characteristic structure is nowadays well understood, the significance of different precipitation-formation processes, such as aggregation and riming, is still unclear. Using a 3-year data set of vertically pointing W-band cloud radar and K-band Micro Rain Radar (MRR) observations from Ny-Ålesund, Svalbard, we statistically assess the relevance of aggregation in Arctic low-level MPCs. Combining radar observations with thermodynamic profiling, we find that larger snowflakes (mass median diameter larger than 1 mm) are predominantly produced in low-level MPCs whose mixed-phase layer is at temperatures between −15 and −10°C. This coincides with the temperature regime known for favoring aggregation due to growth and subsequent mechanical entanglement of dendritic crystals. Doppler velocity information confirms that these signatures are likely due to enhanced ice particle growth by aggregation. Signatures indicative of enhanced aggregation are however not distributed uniformly across the cloud deck, and only observed in limited regions, suggesting a link with dynamical effects. Low Doppler velocity values further indicate that significant riming of large particles is unlikely at temperatures colder than −5°C. Surprisingly, we find no evidence of enhanced aggregation at temperatures warmer than −5°C, as is typically observed in deeper cloud systems. Possible reasons are discussed, likely connected to the ice habits that form at temperatures warmer than −10°C, increased riming, and lack of particle populations characterized by broader size distributions precipitating from higher altitudes.

Plain Language Summary Low-level mixed-phase clouds (MPCs), that is, shallow clouds containing both liquid droplets and ice crystals, form frequently in the Arctic region. Their characteristic structure—consisting of one or multiple liquid layers at sub-zero temperatures, from which ice crystals form and precipitate—is nowadays well understood. However, the processes that lead to the growth of ice crystals into snow have been overlooked. Using a 3-year data set of radar observations from Ny-Ålesund, in Svalbard, Norway, we are able to identify situations when the ice particle growth is dominated by aggregation of several individual crystals. Combining radar observations with temperature information, we find that larger snowflakes are only produced in MPCs if their liquid portion is at temperatures between −15 and −10°C. This coincides with the temperature regime known for favoring aggregation due to growth and subsequent entanglement of branched crystals. Surprisingly, we find no evidence of enhanced ice aggregation at temperatures warmer than −5°C, as is typically observed in deeper cloud systems. Possible reasons are discussed, likely connected to the ice crystal shapes that develop at temperatures warmer than −10°C, increased liquid droplet production, and lack of particles precipitating from higher altitudes.

1. Introduction

Low-level mixed-phase clouds (MPCs) are ubiquitous in the Arctic. They have been shown to occur widely and frequently (e.g., Mioche et al., 2015; Morrison et al., 2012) and to persist typically for several hours (de Boer et al., 2009; Shupe, 2011), with some recorded cases lasting up to several days (e.g., Zuidema et al., 2005). They are further known to introduce, on average, a strong positive surface radiative forcing (Shupe & Intrieri, 2004; Serreze & Barry, 2011; Matus & L'Ecuyer, 2017; Tan & Storelvmo, 2019). Arctic low-level MPCs display a characteristic structure with one or multiple shallow liquid layers close to cloud top, from which ice particles form and precipitate (Shupe et al., 2006). Their persistence is due to a complex interplay of several processes (Morrison et al., 2012), and they have been found to occur under a variety of conditions, including both stable and unstable

stratification, and under a wide spectrum of aerosol concentrations (Gierens et al., 2020; Jackson et al., 2012; Kalesse, de Boer, et al., 2016; Sotiropoulou et al., 2014; Young et al., 2016). Intense cloud-top radiative cooling caused by the supercooled liquid close to cloud top drives buoyant production of turbulence in the cloud layer, which, in turn, drives condensation and maintains the liquid layer (Shupe et al., 2008; Solomon et al., 2011).

Precipitation has been shown to strongly influence many properties of Arctic low-level MPCs. Precipitation, especially when deposited to the surface, withdraws moisture and ice nuclei from the MPC (Morrison et al., 2012; Solomon et al., 2014, 2015). Lower cloud fractions and faster dissipation have been in fact suggested for Arctic stratocumuli that develop precipitation (Harrington & Olsson, 2001; Simpfendoerfer et al., 2019). The modeling experiments by Eirund et al. (2019) have shown that ice precipitation induces thinning and break-up of the organization in Arctic stratocumuli, by generating cold pools at the surface. This effect has been observed to play a role in the transition from mixed-phase stratocumuli to open-cellular convection in cold-air outbreaks (Abel et al., 2017). Avramov and Harrington (2010) further suggested, based on a model sensitivity experiment, that the phase partitioning of Arctic low-level MPCs is strongly sensitive to the assumptions on mass-size, and size-fall speed relations of ice particles, and thus on the ice habits included in the model. It can then be expected that in addition to cloud lifetime, phase-partitioning, and organization, precipitation further affects the radiative characteristics of the MPC (Avramov & Harrington, 2010; Eirund et al., 2019; Harrington & Olsson, 2001; Proske et al., 2021; Solomon et al., 2015; Tan & Storelvmo, 2019). Tan and Storelvmo (2019) have shown that in the Community Earth System Model (CESM) larger ice particles in Arctic MPCs lead to a stronger cloud-phase feedback, that in turn increases the magnitude of Arctic amplification. Gaining process-level understanding of precipitation formation in Arctic low-level MPCs is thus necessary for an accurate model representation of these clouds, including their radiative effects in climate models.

The role of individual ice-growth processes, such as aggregation and riming, in the formation of precipitation in Arctic low-level MPCs is still unclear. In-situ observations of ice particles in Arctic low-level MPCs reported in the literature vary largely: pristine ice crystals, aggregates, and rimed particles have all been observed (Avramov et al., 2011; McFarquhar et al., 2007; Mioche et al., 2017; Wendisch et al., 2019). McFarquhar et al. (2007) reported observing mostly irregular and rimed branched crystals at cloud base, from in-situ aircraft observations at Utqiaġvik, Alaska. At the same site, Avramov et al. (2011) observed dendrites and large aggregates. Mioche et al. (2017) compiled in-situ observations from several aircraft campaigns above the Greenland and Norwegian seas, reporting large fractions of rimed or irregular ice particles. Fitch and Garrett (2022) reported, based on long-term ground-based in-situ observations, that, at Oliktok Point, Alaska, 65% of all frozen precipitation displays some degree of riming, even with observed liquid water path (LWP) of less than 50 g/m^2.

Doppler radar observations at multiple wavelengths can constrain the microphysical processes that determine the formation of precipitation, by providing information on particle fall speed and size. Observations taken at multiple wavelengths can be combined to derive the mean particle size of the hydrometeor population based on their differential scattering properties (Battaglia et al., 2020). The dual-wavelength ratio (DWR), that is, the ratio of equivalent radar reflectivity factors at two separate frequencies, increases when particles grow in size and transition from the Rayleigh scattering regime into the non-Rayleigh scattering regime (e.g., Hogan et al., 2000; Liao et al., 2005). When combined with in-cloud temperature and filtering for intense riming using vertical Doppler velocity information, DWR information has been used to derive the typical temperature regions favoring aggregation for midlatitude clouds by, for example, Dias Neto et al. (2019) and Barrett et al. (2019). These authors observed a first noticeable increase in DWR at Ka-band and W-band to occur in the temperature interval from −15 to −10°C, consistently with early cloud chamber studies (e.g., Kobayashi, 1957). Said temperature region is part of the often-called dendritic-growth zone (DGZ), where several plate-like particle habits are preferentially growing, including dendrites. The DGZ extends from −20 to −10°C, with enhanced depositional growth between −18 and −12°C (Takahashi, 2014; Takahashi et al., 1991). The dendrites' large cross-sectional area and ability to mechanically entangle their branches favor a rapid formation of aggregates (Connolly et al., 2012; Pruppacher & Klett, 2012, Section 14.7). A second enhanced aggregation zone close to 0°C is often observed as well, revealed by a further increase in DWR at several frequency combinations (W-band, Ka-band, Ku-band, and X-band) (Chase et al., 2018; Dias Neto et al., 2019; Tridon et al., 2019). Close to the melting level the presence of a quasi-liquid layer on the ice particles (Fletcher, 1962; Slater & Michaelides, 2019) is thought to favor intense aggregation (Fabry & Zawadzki, 1995).

In this study, we investigate the significance of different ice-growth processes, with a focus on aggregation, for precipitation formation in low-level MPCs at the high Arctic site of Ny-Ålesund, Svalbard, Norway. We obtain a 3-year statistics of DWR in Arctic low-level MPCs, by combining radar observations from a W-band cloud radar and a K-band precipitation radar, and searching the data set for observational fingerprints of ice-growth processes. We combine radar observations with thermodynamic retrievals from a co-located microwave radiometer, to further constrain the thermodynamic conditions that produce said fingerprints. This publication is thus structured as follows: essential theoretical aspects of dual-wavelength radar observations are explained in Section 2, the instruments and further techniques used are described in Section 3, results are shown and discussed in Section 4, and finally the main conclusions and questions raised by this study are summarized in Section 5.

2. Background: Dual-Wavelength Radar Approach

The equivalent radar reflectivity factor Z_e (hereafter called reflectivity) for an ensemble of scatterers in the measurement volume is defined as:

$$Z_e = \frac{\lambda^4}{\pi^5} \|K_W(\lambda)\|^{-2} \int_0^\infty N(\sigma_{b,\lambda})\, \sigma_{b,\lambda} d\sigma_{b,\lambda}, \tag{1}$$

where λ is the transmitted signal wavelength, $\|K_W(\lambda)\|^2$ is the dielectric constant of liquid water, $\sigma_{b,\lambda}$ is the wavelength-dependent backscattering cross-section of the individual scatterers, and $N(\sigma_{b,\lambda})$ its number distribution across the scatterer population (Fabry, 2018, chs. 2 and 3). Therefore, at a given wavelength, Z_e depends on both size (through $\sigma_{b,\lambda}$) and concentration of particles (through $N(\sigma_{b,\lambda})$), in addition to habit, phase, and orientation, and does not provide unequivocal information on particle size. Following the definition of Z_e, values measured at two wavelengths are equal if scattering from all particles and at both wavelengths can be approximated by Rayleigh scattering. If the particles increase in size, they first start to deviate from Rayleigh scattering at the shorter wavelength: this leads to a smaller Z_e at the shorter wavelength compared to the longer one, where more particles are still in the Rayleigh scattering regime (Battaglia et al., 2020). As a result, quantities combining Z_e values at both wavelengths can be related to the characteristic size of the underlying particle size distribution (PSD; Hogan et al., 2000; Kneifel et al., 2016; Liao et al., 2005; Matrosov et al., 2005; Szyrmer & Zawadzki, 2014; Tridon & Battaglia, 2015).

The most commonly used variable to quantify differential scattering of the radar beams at two separate wavelengths is the dual-wavelength ratio (DWR; sometimes named dual-frequency ratio, DFR), defined as:

$$DWR_{\lambda_1,\lambda_2} = \frac{Z_{e,\lambda_1}}{Z_{e,\lambda_2}}, \tag{2}$$

where Z_{e,λ_i} are the equivalent reflectivity factors in linear units and λ_1 is commonly chosen to be larger than λ_2. With this convention DWR = 0 dB if particles scatter according to the Rayleigh regime at both wavelengths and if their $\|K_W(\lambda)\|^2$ (Equation 1) are identical or have been corrected for. DWR values increase as particles transition into non-Rayleigh scattering at the shorter wavelength, then reach a saturation value as non-Rayleigh scattering is reached at both wavelengths. As a result, the DWR can be used as a proxy for the mean size of the sampled particle population (Hogan et al., 2000; Kneifel et al., 2016; Liao et al., 2005). The relation between DWR and particle size is, however, not univocal, and further depends on the particle shape and density (e.g., Matrosov et al., 2019) as well as on the PSD shape (Mason et al., 2019). Using the scattering database of Ori et al. (2021) and dendrite aggregates as well as a simple inverse exponential PSD, we find for example, a DWR_{K-W} of 3 (6, 9) dB to correspond to a mass median diameter of 1.5 (2.4, 3.7) mm, respectively. The maximum DWR value for such modeled dendrite aggregates is 11.4 dB, obtained for a mass median diameter of 8.1 mm, while the saturation DWR value is 9.4 dB. The full dependency of DWR on mass median diameter for different particle types is shown in Appendix A.

Table 1
Selected Technical Specifications of the Three Radar Systems Used in This Study: Two Cloud Radars, JOYRAD-94 and MiRAC-A, and A Precipitation Radar, MRR-2

	JOYRAD-94	MiRAC-A	MRR-2
Central frequency	94.0 GHz	94.0 GHz	24.23 GHz
Time res.	2–3 s	2–3 s	60 s
Integration time	0.5–0.6 s	0.5–0.6 s	60 s
Range res.	3.2–7.5 m	3.2–7.5 m	30 m
Min. range	100 m	100 m	30 m
Max. range	12 km	12 km	960 m
Sensitivity at 100 m	−62 dBZ	−64 dBZ	−13 dBZ
Sensitivity at 900 m	−50 dBZ	−50 dBZ	−6 dBZ
Beam width (half power)	0.5°	0.85°	1.5°

Note. Further information on the instruments can be found, respectively, in Küchler et al. (2017), Mech et al. (2019), and Klugmann et al. (1996).

3. Data Sets and Methods

3.1. Measurement Site

The observations analyzed in this study were obtained at the observatory of the Arctic research base AWIPEV in Ny-Ålesund, Svalbard. Ny-Ålesund is located at 79°N, in the region where Arctic amplification is the most intense (e.g., Dahlke & Maturilli, 2017). The site is located 13 m above sea level close to the coast of the Kongsfjorden, a fjord with surrounding mountains with altitudes of 500–1,000 m. Similar to other locations in the Arctic, the lower troposphere above Ny-Ålesund is often stably stratified. Temperature and humidity inversions have been found in respectively 75% and 84% of the daily radiosondes launched between 1993 and 2014 (Maturilli & Kayser, 2017). Mean monthly values of surface air temperature have been observed to range between 5.8°C in July and −12.0°C in March (Maturilli et al., 2013) and average yearly precipitation has been measured to be 564 mm/year with a large standard deviation of 444 mm/year, in the 2012–2019 period (Mori et al., 2021). Furthermore, remote sensing observations of clouds at this location have already been analyzed in depth by previous studies, such as Nomokonova, Ebell, et al. (2019), Vassel et al. (2019), Nomokonova et al. (2020), Gierens et al. (2020), and Ebell et al. (2020).

The characteristics of low-level MPCs at Ny-Ålesund have been reported by previous studies, in particular by Nomokonova, Ebell, et al. (2019) and Gierens et al. (2020). Their statistics display similar low-level MPC characteristics, compared to what has been observed at other Arctic sites, such as during the Surface Heat Budget of the Arctic Ocean (SHEBA) campaign (Shupe et al., 2006), at Utqiaġvik, Alaska (de Boer et al., 2009; Zhao & Wang, 2010), and at Eureka, Nunavut, Canada (de Boer et al., 2009). Nomokonova, Ebell, et al. (2019) observed a frequency of occurrence of 20.6% for single-layer MPCs (with no restriction on cloud depth or cloud-top height). They report an average LWP of 66 g/m^2, and average ice water path (IWP) of 164 g/m^2 for this cloud type. Gierens et al. (2020) estimated the occurrence of low-level MPCs lasting more than 1 hr to be 23%, with average LWP and IWP values of 35 and 12 g/m^2, respectively. The height of the liquid base of low-level MPCs ranges typically from 0.54 to 1.0 km, which is at or above the height of the surrounding mountaintops (Gierens et al., 2020).

3.2. Radar Systems

In this study, we calculate DWRs (K-band and W-band) of MPCs based on continuous zenith-pointing radar observations available from September 2017 to October 2018, and from June 2019 to February 2021. The W-band observations are obtained with 94-GHz frequency-modulated continuous wave (FMCW) Doppler cloud radars (RPG-FMCW-94-SP, manufactured by Radiometer Physics GmbH [RPG]; Küchler et al., 2017). Observations from two slightly different RPG-FMCW-94-SP radar systems have been combined: during the first time period, observations were collected with the MiRAC-A (Mech et al., 2019) which has a slightly larger beamwidth than the JOYRAD-94 (Küchler et al., 2017), used from June 2019 onwards. Both systems collected data with a temporal resolution of 2–3 s and vertical resolutions between 3 and 8 m depending on the range region (for technical details of the radars see Table 1, Küchler et al. (2017), and Gierens (2021)). The measurements were set up with a minimum and maximum range of 100 m and 12 km, respectively.

The W-band observations are complemented by observations from a K-band (24 GHz), zenith-pointing, FMCW Doppler Micro Rain Radar (MRR-2; Metek GmbH; Klugmann et al., 1996). Due to its economic and light-weight design, it has been frequently used to study snowfall in mountainous (Cha et al., 2009; Kneifel et al., 2011) and polar regions (Durán-Alarcón et al., 2019; Grazioli et al., 2017), evaluate satellite products (Maahn et al., 2014; Souverijns et al., 2018) and model performance (Scarchilli et al., 2020). We use the processing method developed by Maahn and Kollias (2012), which is fine-tuned for observations of frozen hydrometeors. The resolution in time (60 s) and range (30 m) is much coarser than the W-band cloud radars. Its average sensitivity for this measurement setup ranges between −13 and −6 dBZ, depending on range. Said sensitivity was calculated as the mean average

noise level times 1.2, as that is the lowest threshold for spectral reflectivity values to be considered as signal in the processing routine by Maahn and Kollias (2012).

To calculate DWRs, we averaged the W-band data to the MRR resolution. The reflectivity from the W-band cloud radars was averaged in linear scale, then converted to decibel. Note that during the study period, the MRR was set up to measure with a maximum range of 960 m. Calculated DWRs are therefore only available from the lowest W-band range gate (100 m) up to this height. DWR was not corrected for liquid attenuation, due to the typically low amounts of liquid observed in low-level MPCs in the Arctic. Only 24.2% of the MPC events detected by the MRR in fact displayed LWP higher than 150 g m^{-2} (see Section 4.1), which leads to a total two-way attenuation of approximately 1.2 dB at W-band, according to Tridon et al. (2020). Furthermore, in most of the analysis, we focus on the DWR value at the base of the liquid layer of the MPC, where the radar signal has undergone negligible attenuation. Mean Doppler velocity (MDV) was taken from the W-band cloud radars, and was also averaged to the same time and range resolution as the MRR. To analyze DWR and MDV in a consistent manner, MDV values above the maximum range of the MRR were ignored.

3.2.1. Radar Calibration Evaluation

Since the aim of our analysis is gaining information on particle size based on DWR calculated from Z_e at K-band and W-band, evaluating the calibration (especially in a relative sense) of all radar systems involved is necessary. The radar calibration constant might change, for example, due to drifts, which can lead to biases in the measured Z_e. In our analysis, we obtained calibration offsets for the MRR following a disdrometer-based approach (e.g., Dias Neto et al., 2019; Myagkov et al., 2020). The W-band radars were instead calibrated using a DWR-based approach, requiring that the DWR distribution for observations of Rayleigh targets only has its mode at 0 dB. All the derived offsets are reported in Table B1 in Appendix B.

At the AWIPEV site, a Parsivel disdrometer (Löffler-Mang & Joss, 2000) is installed, and data are available for the whole study period. Parsivel measures volume-equivalent sizes and fall speeds of particles that fall through its laser beam. It thus provides PSDs, and fall speed distributions of the particle population. A critical assessment of its performance can be found in Battaglia et al. (2010). The disdrometer-based calibration method consists in forward simulating Z_e values from drop size distribution (DSD) observed by Parsivel during rain events. The simulated reflectivities were then compared with the observed ones, taken from the range gate between 120 and 150 m. We selected the rain events based on the following criteria:

1. The disdrometer detects liquid precipitation. If frozen precipitation is detected all liquid within 10 min is ignored.
2. Only data from June through September are used, and only when surface temperature (from nearby weather station) is greater than 5°C, to exclude misclassified frozen or partially melted precipitation.
3. Disdrometer data are only used if rain rate ≥0.1 mm/hr following the approach by Williams et al. (2005). Additionally, only measurements containing at least 25 samples per minute are used. Both criteria are required in order for the disdrometer measurements to be representative of the drop population.
4. DSDs from Parsivel must contain particles larger than 1 mm. This criterion was determined following Myagkov et al. (2020), so that evaporation of the drops between the chosen range gate and the ground does not affect the forward simulated Z_e values.
5. Events are required to last at least 1 hr, with gaps allowed for a total of one sixth of the duration of the event.

Reflectivity values were based on the observed DSDs, and forward simulated with the T-matrix method (Leinonen, 2014; Waterman, 1965), using a drop shape model from Thurai et al. (2007). Following Huang et al. (2008), the drops were assumed to have Gaussian distributed canting angles, with 0° mean value and a 10° standard deviation. Attenuation coefficients were calculated using the same approach, and were multiplied by twice the height of the used range gates. The path-integrated attenuation was then subtracted from the forward simulated reflectivity values. All Z_e values below −10 dBZ and above 25 dBZ were excluded. It should be noted that we did not compare time series of observed and simulated Z_e but rather compared the Z_e distributions of the total rainfall event. This mitigates the issue of time delays between Z_e observed at the lowest radar range gate and the surface observations. A single median reflectivity value was then obtained for all events in each June-through-September period, for both the observations and the forward simulation. In each period, the Z_e offset was obtained by subtracting the two median values. In the periods from October to May, monthly Z_e offset values were calculated by linearly interpolating the obtained values.

We attempted to apply the same disdrometer-based approach to the calibration of the W-band radars, but we observed a strong dependence of the calculated offset values on the accumulated precipitation during the events (not shown). We hypothesize that this is due to deterioration of the coating of the radomes, leading to the radomes taking in some rain water, thus causing increasing attenuation of the signal. Although this phenomenon is not an issue for snowfall observations, it hampers the applicability of the disdrometer-based method to the W-band radars. For the MRR, we did not observe any attenuating effect due to wet antenna. Unlike the W-band radars, the MRR is not covered by a radome. Due to this reason, we used the calibrated MRR as our reference and estimated the offsets of the W-band radars using a DWR-based approach in light snowfall. This approach using light snowfall is overall similar to relative calibration methods applied to cloud radar observations of low-reflectivity Rayleigh-scattering hydrometeors by Hogan et al. (2000), Dias Neto et al. (2019), and Tridon et al. (2020). The relative offset estimated with this approach uses the fact that, for observations of Rayleigh-scattering frozen hydrometeors only, the DWR is approximately 0 dB. Rayleigh-scattering hydrometeors are typically selected by requiring that the radar reflectivity at the longer wavelength is below a certain threshold: for example, Dias Neto et al. (2019) used a threshold of −10 dBZ in Ka-band reflectivity when calibrating a W-band radar. In our case, due to the low sensitivity of the MRR such a low threshold could not be used. Therefore, selecting MRR echoes of solely Rayleigh targets was not possible. Nonetheless, Matrosov et al. (2019) reported scattering calculations, as well as observations from the Arctic site of Oliktok point, Alaska, of DWR of frozen hydrometeors at Ka-band and W-band, showing that for Ka-band reflectivities between −5 and 0 dBZ, the DWR distribution has its peak close to 0 dB, and is thus associated with Rayleigh scattering. Therefore, the radar measurements used in the calibration were selected with the following criteria:

1. Signal corresponds to ice-only clouds, based on the Cloudnet target classification (see Section 3.3).
2. Z_e from MRR is between −5 and 0 dBZ.
3. If Parsivel detects liquid precipitation, all echoes within 10 min are ignored.

Monthly DWR distributions for observations satisfying these conditions were then obtained, and the mode of the distribution was taken as monthly Z_e offset. Following the results by Matrosov et al. (2019), this calibration approach rests on the assumption that the monthly DWR distributions are characterized by a peak associated with Rayleigh scattering, and a tail on the right side of the peak, associated with non-Rayleigh scattering. The mode of the distribution was chosen as offset, so that, after applying the offset, the peak of the distribution is centered around a DWR value of 0 dB. The bins used to calculate the distributions are 0.5 dB wide. We estimated the uncertainty associated with this calibration approach by taking the left standard deviation of the monthly DWR distributions with respect to the mode. The root mean square value of such monthly uncertainties is 2.1 dB. An example further illustrating the DWR calibration and uncertainty calculation procedure is given in Appendix B.

3.3. Temperature Soundings and Hydrometeor Classification

Many microphysical processes are known to be strongly dependent on temperature (e.g., Pruppacher & Klett, 2012, chs. 9, 13, and 14), we thus investigate the dependence of DWR statistics on in-cloud temperature, as well as cloud-top and cloud-base temperature. Additional information on cloud phase is also needed, to properly identify MPC events. For these reasons, we use temperature profiles retrieved from a HATPRO (Humidity And Temperature PROfiler; Rose et al., 2005) microwave radiometer, and the Cloudnet target classification product (Hogan & O'Connor, 2004; Illingworth et al., 2007). The HATPRO is operated by the Alfred Wegener Institute (AWI) and measures on the same platform as the radar systems. In addition to temperature soundings, HATPRO observations are also used to retrieve LWP. To increase the accuracy of temperature profiles especially in the lowest 1 km, the observations at seven channels along the 60 GHz oxygen absorption band are obtained at various elevation angles (Crewell & Lohnert, 2007). Elevation scans are regularly performed every 15–20 min. The profiles are linearly interpolated in time to the same resolution as the MRR (60 s). Gierens et al. (2020) assessed the uncertainty of these temperature retrievals in low-level MPCs against radiosondes (see their fig. 3c), and found an RMSE of 0.7K at the surface, that increases to 1.6K (2.0K) at the liquid base of the MPC (cloud top).

Observations from the W-band cloud radar, HATPRO, and a ceilometer (model Vaisala CL51; Maturilli and Ebell (2018)), together with output from the ICOsahedral Nonhydrostatic weather model (ICON; Zängl et al. (2015)), in its global numerical weather prediction mode (ICON-IGLO), are operationally combined into the Cloudnet product (Hogan & O'Connor, 2004; Illingworth et al., 2007). In particular, we use the target classification product which classifies hydrometeors into: cloud droplets, supercooled cloud droplets, and cloud ice,

as well as drizzle or rain. The presence of liquid at sub-zero temperatures is mainly based on ceilometer observations. The ceilometer signal undergoes far greater attenuation when traversing a cloud layer containing cloud droplets, compared to an ice layer, because of the droplets' far higher number concentration. This leads to limitations of the Cloudnet product if more than one liquid layer is present, as often the pulse is unable to penetrate the lowest liquid layer. We will henceforth use the term *liquid base* to refer to the base of the lowest liquid layer detected by the ceilometer. We will further refer to the portion of the MPC above the liquid base as *mixed-phase layer* (MPL). In this study, we use the Cloudnet target classification product to derive the height of the liquid base, and cloud-top height.

3.4. Selection of Mixed-Phase Cloud Events

Low-level MPC events were identified following an approach similar to that employed by Gierens et al. (2020). The events were detected using the following criteria:

1. Cloud top is at or below 2,500 m.
2. If multiple cloud layers are present below 2,500 m, they are considered as one if separated by 60 m or less, otherwise only the lowest layer is included in the analysis, and the remaining ones are excluded.
3. Cloudnet indicates the presence of both liquid and ice in the cloud layer.
4. Liquid and ice are present for at least 60 min, with gaps allowed for a total of one sixth the total duration of the event.

During intense precipitation events, snow might accumulate on the ceilometer aperture, thus leading to ceilometer data not being available, and liquid layers not being identified in the Cloudnet target classification. Under these conditions, criterion three is not satisfied even though a low-level MPC is present. When the ceilometer signal is not available, the presence of liquid was evaluated using the LWP retrievals from HATPRO: an LWP threshold of 10 g/m^2 was used.

Using this approach, we identified a total of 1,605 low-level MPC cases, adding up to a total duration of 7,592 hr. Out of these, 1,042 cases, or 6,022 hr, were detected by the MRR. Out of all cases (cases detected by the MRR), 23.6% (25.6%) were detected in winter, 15.4% (18.0%) in spring, 30.2% (23.0%) in summer, and 30.8% (33.4%) in autumn. We would like to highlight that different subsets of all detected events were used in different parts of the analysis. In Sections 4.3 and 4.4, the value of DWR at liquid base, and its maximum value below the liquid base are evaluated in each sample. When evaluating these quantities, only the subset of data where the ceilometer signal is available and the liquid base is within the MRR range was used. In Section 4.4, we only focus on MPC events detected by the MRR, and with surface temperature colder than 0°C: 508 cases satisfy these conditions.

4. Results and Discussion

A typical low-level MPC event observed from February 4 to 6, 2021 is displayed in Figure 1. The four panels depict Z_e and MDV from the W-band cloud radar, DWR, and LWP. The figure also shows the height of the liquid base and temperature contours, derived from the ceilometer and HATPRO, respectively. The event depicted in the figure produced precipitation characterized by a wide range of DWR values. In particular, the MPC produced high DWR showers intermittently throughout its duration, highlighting the presence of large ice particles. These high DWR showers are alternating with regions characterized by lower DWR values, and even periods when the reflectivity was below the sensitivity of the MRR, and thus DWR values were not available. Figure 1 shows that most high DWR showers originate from within the mixed-phase layer. Interestingly, high DWR values are not necessarily linked to high reflectivity values, and vice versa.

4.1. Impact of MRR Sensitivity and Limited Maximum Range on Detected Cloud Characteristics

In the following analysis, we will focus only on MPC events detected by the MRR. The two limitations of the MRR are its maximum range (960 m), and lower sensitivity compared to the W-band cloud radars. To evaluate the effect of these limitations on the data sampled for the analysis, characteristics of MPCs detected by the MRR, and MPCs detected only by the W-band cloud radars are shown and compared in Figure 2. Overall, MPCs detected by the MRR tend to last longer (median 4.0 hr) and display higher LWP values (median 69.1 g/m^2) compared to events not detected by the MRR (2.0 hr and 23.0 g/m^2, respectively). Figure 2f further shows that

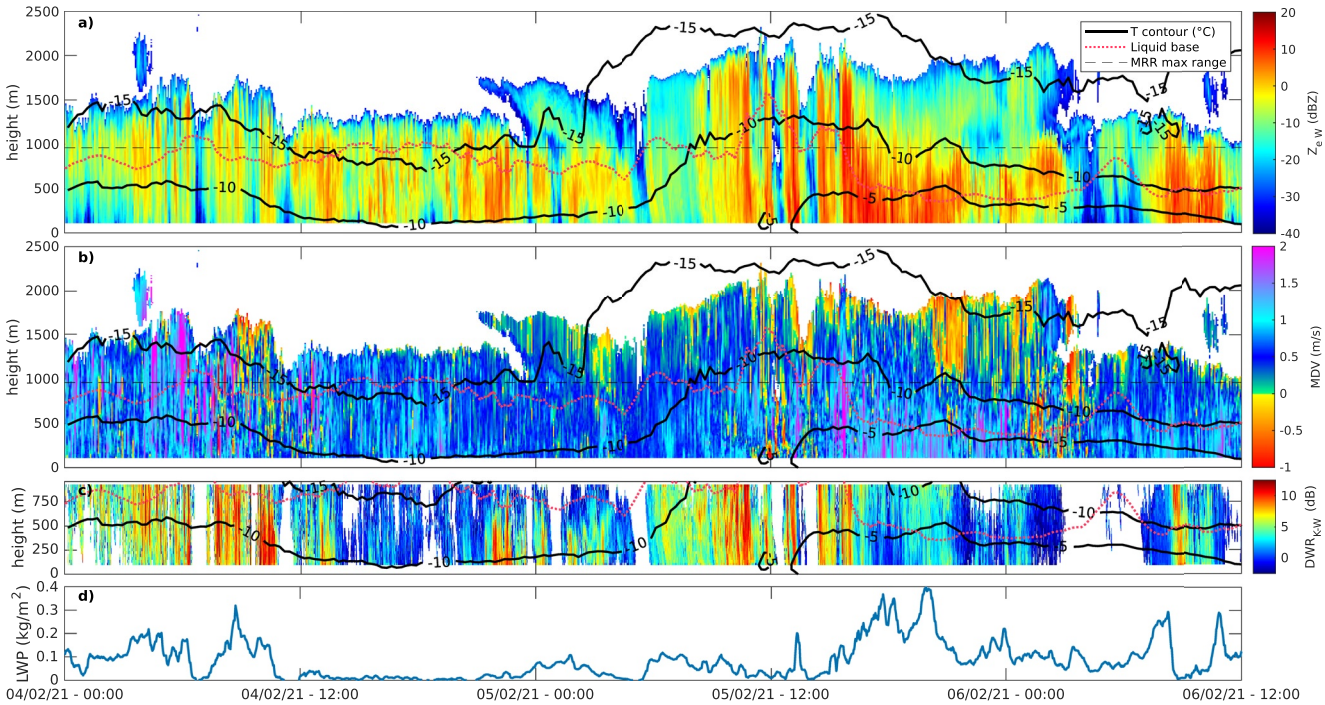

Figure 1. Example of low-level mixed-phase cloud event observed in Ny-Ålesund on February 4–6, 2021. Panels (a) and (b) display the reflectivity and mean Doppler velocity measured by the W-band cloud radar, respectively. Panel (c) depicts the dual-wavelength ratio obtained from Micro Rain Radar (MRR) and cloud radar observations. Panel (d) displays the liquid water path, retrieved from HATPRO microwave radiometer observations. In panels (a–c), contour lines indicate temperature (black) based on retrievals from HATPRO, and the liquid base height (pink dotted) from the Cloudnet target classification product. The horizontal dashed line in panels (a) and (b) indicates the maximum range of the MRR. Times indicated are in UTC.

MPC events detected by the MRR tend to have colder cloud-top temperature (CTT; median −9.8°C), compared to the events only detected by the W-band cloud radars (−8.2°C). Out of all events with CTT between −20 and −10°C, the MRR detects 84.8% of them, while it detects 75.6% of all events with CTT warmer than −10°C. Moreover, the number of MPC events with CTT colder than −20°C identified during the study period is very low (93), and 81.5% of these clouds are detected by the MRR. While 66.2% of MPCs detected by the MRR have their liquid base within the instrument's maximum range, only 12.4% have their top within it (as shown in Figures 2c and 2d). For this reason, the analysis reported in the following sections focuses on precipitation observed at, and below, the liquid base of MPCs. The limited range of the MRR does not appear to introduce a significant bias in the cloud-top height of the detected cases, as the median values for MPC events detected by the MRR is 1,431 m, while that for events not detected by the MRR is 1,341 m. This does not hold true for liquid-base height, as the median value for MPC events detected by the MRR is 791 m, while that for events not detected by the MRR is 1,001 m. The mixed-phase layer depth distributions in Figure 2e, calculated as the difference between cloud-top height and liquid-base height, suggest that this discrepancy in liquid-base height can be mainly attributed to shallower MPCs not being detected by the MRR. The median MPL depth for events detected by the MRR is in fact 480 m, while that for events not detected by the MRR is 280 m.

In summary, the lower sensitivity of the MRR leads to the detection of events that produce higher reflectivities: these events appear to be characterized by a longer duration, higher LWP values, deeper MPLs, and colder CTTs. The limited range of the MRR seems to introduce a bias toward events with lower liquid-base height. Interestingly, a similar bias is not observed in cloud-top height, suggesting that the MPCs causing said bias in liquid-base height are rather shallow, and likely characterized by a low reflectivity as well.

4.2. Characteristic Sizes and Fall Speeds of Precipitating Ice Particles in the Lowest 1 km

In Figure 3, we show long-term statistics of DWR and MDV (taken from W-band cloud radar) as function of temperature, in the detected low-level MPC events. This approach is similar to what has been applied to

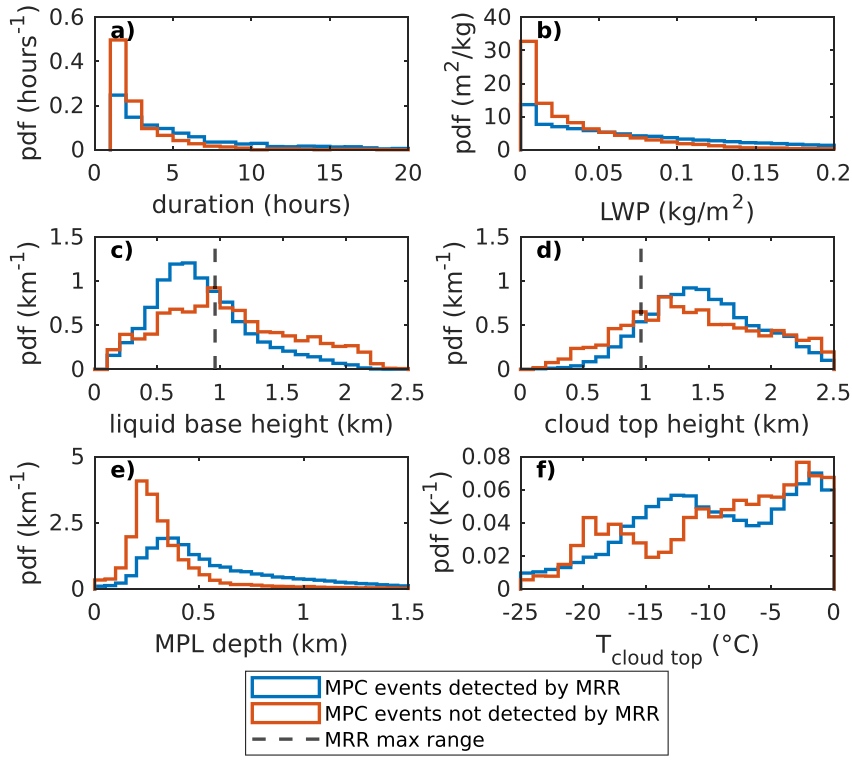

Figure 2. Statistics of mixed-phase cloud characteristics in Ny-Ålesund. Probability density functions (PDFs) are shown for events detected by the Micro Rain Radar (MRR), and for events that were not detected by the MRR, and thus were only detected by the W-band cloud radar. The parameters shown are MPC event duration (a), liquid water path (LWP; b), liquid-base height (c), cloud-top height (d), mixed-phase layer depth (e), and cloud-top temperature (f). The dashed lines in panels c and d indicate the maximum range of the MRR. Bin sizes are respectively: 1 hr, 10 g m^{-2}, 100 m, 100 m, 50 m, 1°C.

triple-wavelength observations in midlatitude clouds by Dias Neto et al. (2019) and Ori et al. (2020). The main difference in our study is that we focus on low-level MPCs and are restricted to the lowest 960 m, as well as clouds that produce large enough Z_e signals to be detected by the MRR. The DWR and MDV statistics in Figure 3 are displayed as contoured frequency by temperature diagrams (CFTDs; Yuter & Houze, 1995). Here, DWR and MDV values are matched with temperature (T) retrieved at the same height, and the figure displays joint histograms of DWR and T (panel a), and MDV and T (panel b). These histograms are normalized to one at each chosen T level. Note that, unlike many other studies where CFTDs are employed, panels (a) and (b) in Figure 3 should not be interpreted as continuous profiles. Because of the limited depth of low-level MPCs, and the limited range of the MRR, each available profile only spans a portion of the displayed temperature range. The mean temperature difference between the lowest W-band cloud radar range gate (100 m), and the highest MRR range gate (960 m) is 5.2°C, with 1.8°C standard deviation. The total number of samples (Figure 3c) reveals that 90% (95%) of observations occur at temperatures higher than −12.7°C (−15.1°C), with maxima at −10 and 0°C.

Figure 3 displays that at temperatures colder than −15°C median DWR values are close to 1 dB, corresponding to median sizes smaller than 1 mm. Median DWR then rapidly increases to 4.1 dB between −15 and −12°C. These enhanced DWR signals can be found at temperatures as high as −6°C, with a distinct maximum between −12 and −8°C (5.6 dB). At temperatures close to 0°C, the median DWR decreases back to lower values, with a median of 2.7 dB between −5 and 0°C. Similarly, median MDV in Figure 3b has a relatively constant value of 0.6 m/s between −20 and −12°C, typical for small ice crystals (Barthazy & Schefold, 2006; Heymsfield & Westbrook, 2010; Kajikawa, 1972; Mitchell, 1996), grown most likely by vapor deposition. At the −13°C level where the DWRs increase, we also find the MDVs to increase. Interestingly, while the DWRs seem to remain almost constant between −12 and −8°C, the MDVs steadily increase, reaching values close to 1 m/s, which is a typical terminal velocity of larger aggregates (Brandes et al., 2008; Heymsfield et al., 2007; Karrer et al., 2020; Locatelli & Hobbs, 1974). A similar behavior in terms of both DWR and MDV can be noticed in the case study in Figure 1 as well. Combining DWR and MDV information, together with previous knowledge from

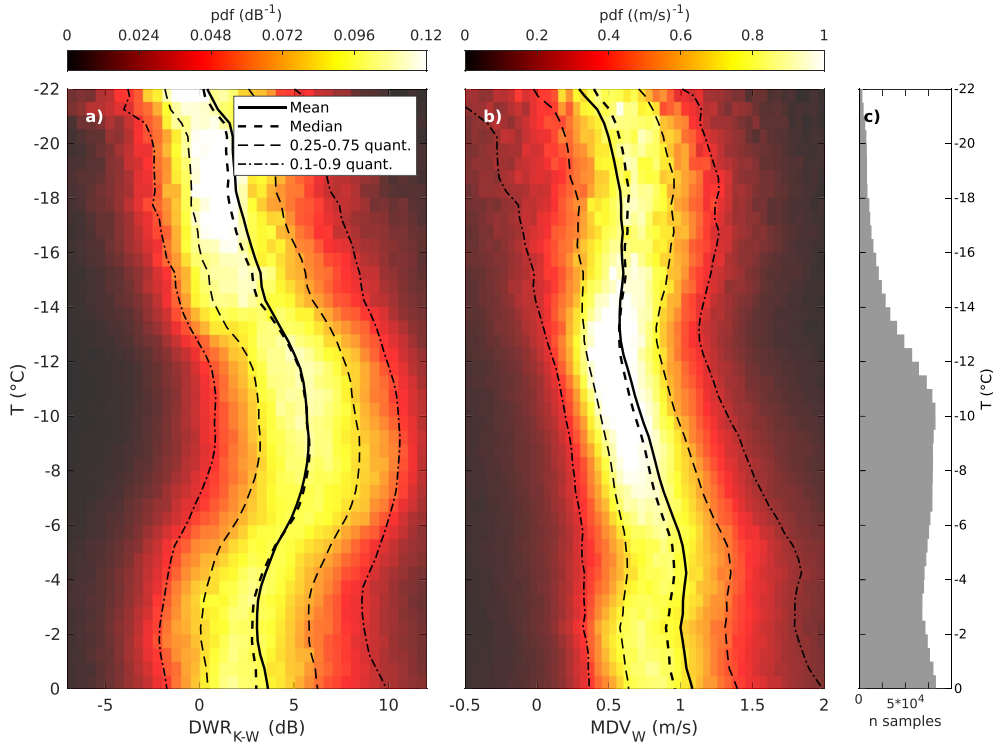

Figure 3. Contoured frequency by temperature diagram (CFTD) of dual-wavelength ratio (DWR; panel a) and mean Doppler velocity (MDV; panel b) in the detected mixed-phase cloud events. Panel (c) displays the number of samples available at each temperature level. MDV values are only included if Micro Rain Radar (MRR) echoes are available. Bin sizes are: 1 dB, 0.05 m/s, and 0.5°C.

midlatitude clouds, we thus hypothesize that aggregation might play an important role in the formation of the high DWR hydrometeors we observe between −15 and −5°C. The region of increasing DWR starting at −15°C is likely associated with rapid depositional growth of branched dendritic particles in the DGZ, which subsequently aggregate. An increase in DWR associated with enhanced aggregation in the DGZ has been previously observed in midlatitude clouds (Barrett et al., 2019; Dias Neto et al., 2019; Lamer et al., 2021; Ori et al., 2020; Oue et al., 2021). The presence of high DWR particles at temperatures warmer than −10°C in Figure 3a could be simply a result of particles that mainly aggregated in the DGZ and then sedimented to warmer temperatures, while continuing to aggregate.

The low fall velocities observed in Figure 3b at temperatures colder than −5°C are not indicative of severe riming that could explain the observed DWRs. However, we cannot rule out the possibility of light riming of the larger aggregates, as well as smaller rimed particles, as their terminal fall velocities could overlap with the fall velocity of larger, unrimed aggregates. Riming has in fact been observed to occur frequently in Arctic MPCs (Fitch & Garrett, 2022; McFarquhar et al., 2007; Mioche et al., 2017). However, the MDVs from 72.3% (82.7, 91.6%) of the observed echoes are slower than 1.0 m/s (1.2, 1.5 m/s) between −15 and −5°C, which corresponds to a rime mass fraction of 0.31 (0.47, 0.65) according to Kneifel and Moisseev (2020). It further appears unlikely that the DWR increase at −15°C is mainly driven by riming: first, we are not aware of any evidence that riming preferentially occurs at −15°C. Second, in this temperature regime, the Wegener-Bergeron-Findeisen process has its maximum (Korolev & Mazin, 2003) and has been shown to hamper the formation and survival of liquid droplets (Silber et al., 2021).

Although the DWRs at temperatures warmer than −5°C decrease back to lower values (median of 2.7 dB between −5 and 0°C), the MDVs remain almost constant, close to 1 m/s (median of 1.1 m/s between −5 and 0°C). One potential explanation for this signature could be the higher terminal fall velocity of needle particles, which, together with columns, preferentially grow at temperatures higher than −10°C by vapor deposition (e.g., Bailey & Hallett, 2009). They can reach terminal velocities close to 1 m/s at smaller sizes compared to plate-like particles

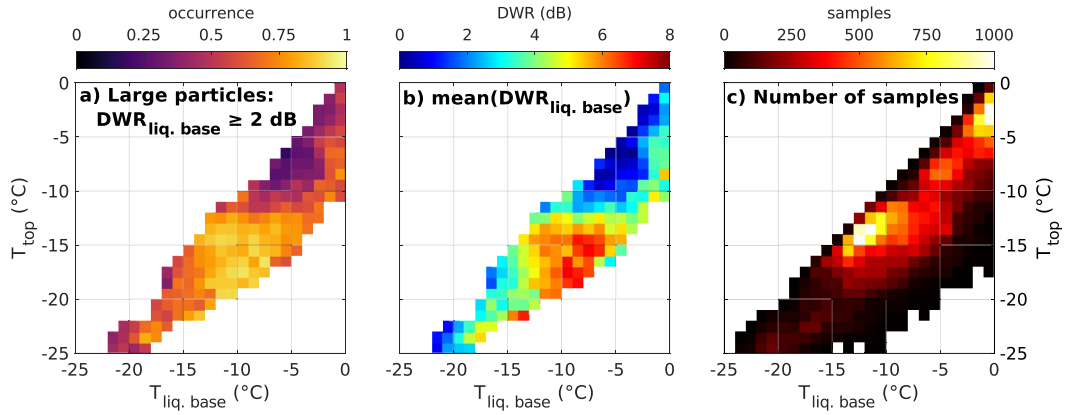

Figure 4. Frequency of occurrence of dual-wavelength ratio (DWR) above 2 dB at liquid base (a), mean DWR at liquid base (b), and number of samples at liquid base (c) as function of cloud-top and liquid-base temperature. In panels (a) and (b), bins with less than 60 total samples are ignored. Bins are 1°C wide.

(Kajikawa, 1972; Mitchell, 1996). Also, the presence of supercooled drizzle and potential enhanced riming of smaller ice particles with low DWR could explain the observed behavior. The likelihood for the formation of drizzle and intensified riming has been found to strongly increase at temperatures closer to the melting level (Cortinas Jr et al., 2004; Kneifel & Moisseev, 2020; Zhang et al., 2017). Overall, the DWR-MDV behavior found for MPCs at temperatures close to 0°C is significantly different from what is observed at the midlatitudes. Several studies observed a second and even stronger DWR increase from −5°C toward the melting level (Chase et al., 2018; Dias Neto et al., 2019; Ori et al., 2020; Tridon et al., 2019). Interestingly, we are able to find a similar behavior also in Ny-Ålesund in cloud systems that are deeper than 2.5 km, as shown in Appendix C. The lack of aggregation close to the melting level in the detected low-level MPC events is further explored in the next section.

4.3. Precipitation Formation in the Mixed-Phase Layer

In the previous section, we analyzed DWR values with respect to temperature retrieved at the same height. We can assume that in low-level MPCs, the main nucleation and initial depositional growth takes place in the mixed-phase layer (MPL), where on average saturation with respect to liquid water is reached. Therefore, we investigate how much the particles already aggregate in the MPL and how relevant the temperature of the MPL is for the occurrence of larger aggregates in the entire profile.

We analyze the DWRs observed at the liquid-base height, and relate it to the cloud-top and liquid-base temperatures in Figure 4. For a simpler interpretation, in panel a, we group the profiles into small particles (DWR at liquid base lower than 2 dB, corresponding to a mass median diameter of approximately 1.3 mm; see Figure A1 in Appendix A) and larger particles (DWR at liquid base equal or higher than 2 dB), that are most likely a result of aggregation and/or riming. The threshold of 2 dB was also chosen because of the estimated uncertainty on DWR of 2.1 dB. DWR values higher than 2 dB can thus confidently be attributed to non-Rayleigh scattering by hydrometeors. We also tested slightly different DWR thresholds but did not find a substantial impact on the results (not shown). Figure 4a thus shows the frequency of occurrence of DWRs at liquid base higher than 2 dB. Panels (b) and (c) in the figure display the mean DWR value at liquid base, and number of available samples, respectively, both as function of liquid-base temperature and CTT.

Figure 4a illustrates that large particles appear to mainly originate from mixed-phase layers with liquid-base temperature higher than −15°C and CTT lower than −10°C. In this temperature regime, 76.8% of the samples in fact display DWRs at liquid base of 2 dB or larger. The mean DWR value at liquid base (Figure 4b) also illustrates that even very thin MPLs on average generate particles with DWRs of 5 dB or higher, if they contain temperatures of −13 to −14°C. Interestingly, this overlaps with the −15.5 to −13.3°C interval, where the laboratory study by Takahashi (2014) observed the maximum growth rate of plate-like crystals. As expected, if the MPL is thicker (larger difference between cloud-top and liquid-base temperature), also the mean DWRs increase, because of the longer time particles can grow by deposition and subsequent aggregation.

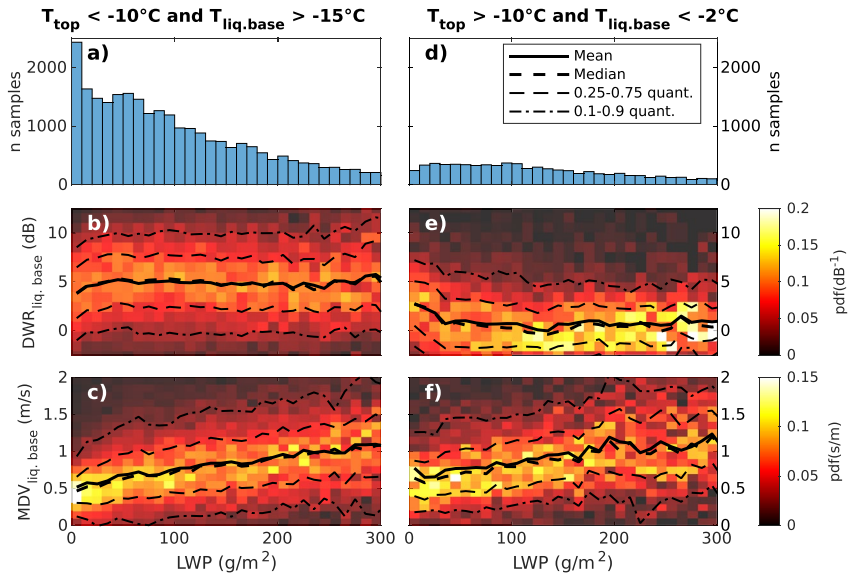

Figure 5. Liquid water path (LWP) distribution (a, d), and joint LWP-DWR (b, e), and LWP-MDV (c, f) distributions for mixed-phase cloud (MPC) events in two distinct regimes. Panels (a–c) include MPC events whose mixed-phase layer is at least partly in the temperature interval between −15 and −10°C. Panels (d– f) include MPC events whose mixed-phase layer temperature does not exceed −2°C and does not succeed −10°C. The joint distributions in panels (b, c, e, and f) are normalized to one in each LWP bin. Bin widths are: 5 g/m^2, 0.5 dB, and 0.05 m/s.

Figure 4b shows that enhanced DWR values can also be found in MPLs at temperatures colder than −15°C (i.e., liquid-base temperature colder than −15°C in the figure), namely temperatures belonging to the colder portion of the DGZ, or colder than the DGZ completely. However, the mean DWR and overall frequency of occurrence are generally much lower than what we observe when temperatures between −15 and −10°C are observed in the MPL: this is clearly indicated by the low number of samples in Figure 4c for cases with liquid-base temperature colder than −15°C. Interestingly, for the events with liquid-base temperature colder than −15°C, the MPL also needs to be deeper (i.e., larger temperature difference between cloud top and liquid base) to produce enhanced DWRs.

The dependence of DWR and MDV at liquid base on LWP is shown in Figure 5, for two separate temperature regimes. Enhanced aggregation in the −10 to −15°C temperature region appears to occur already at relatively small LWP values. No substantial change in DWR is found for increasing LWP. This independence can be interpreted as a proof that the observed DWR signature is mainly caused by aggregation rather than riming as the latter would be expected to increase with LWP. However, Figure 5c shows that the MDV observed at the liquid base continuously increases with larger LWP. We suspect that, while riming is not the main mechanism that increases DWR, it is still contributing to the observed increasing particle fall speeds by increasing ice particle density.

4.3.1. Discussion: Rapid Depositional Growth and Subsequent Aggregation in the DGZ

The preferential growth of dendrites in the DGZ is thought to lead to a more efficient aggregation, compared to other temperature regions (Pruppacher & Klett, 2012, Section 14.7), although many details of these processes are still not thoroughly understood. We believe that the signatures found in this study are particularly valuable to better constrain the process of dendritic growth and subsequent aggregation. Unlike in deeper clouds, no particles from above enter the DGZ in the low-level MPCs that are the focus of this study. Instead, we can assume that all ice particles are nucleated and grown within the relatively narrow region of the mixed-phase layer. We can further assume that the majority of particles in the MPL grow in conditions that are close to liquid water saturation. This allows to compare and relate our results directly to recent laboratory experiments investigating depositional growth (Takahashi, 2014) or aggregation (Connolly et al., 2012) in the temperature regime of the DGZ.

A number of factors are known to be mainly responsible for the rapid formation of aggregates in the DGZ. Here, the maximum difference between liquid and ice saturation pressures is found (Pruppacher & Klett, 2012), and a maximum of the Wegener-Bergeron-Findeisen (WBF) process is observed (Korolev, 2007). At these

temperatures, if high enough ice supersaturations are reached, ice particles grow into dendritic shape (Bailey & Hallett, 2009; Pruppacher & Klett, 2012, Section 13.3), which is connected to enhanced capacitance (Westbrook et al., 2008; Pruppacher & Klett, 2012, Section 13.3) and ventilation coefficients (Takahashi et al., 1991). All these effects together lead to a maximum in the water vapor depositional growth on ice particles in this temperature region (Takahashi, 2014; Takahashi et al., 1991). As already mentioned, Takahashi (2014) found that the depositional growth rate is maximized between −15.5 and −13.3°C (see their Figure 6). After a growth time of 10 min, they observed particles reaching maximum sizes of 1.5–1.8 mm with preferentially stellar, dendritic or fern-like habits. This temperature region coincides with the MPL temperatures where we observed the largest DWRs in Figure 4b.

In addition to the very favorable depositional growth conditions, the slower terminal fall velocities of dendrites compared to other shapes with similar mass (e.g., Kajikawa, 1972; Mitchell, 1996) allow them to stay in the supersaturated layer of the cloud for a longer time compared to other ice habits. For example, a 1 mm dendrite falls at 0.3 m/s while the same sized column, which grows for example, at temperatures higher than −10°C, has a terminal velocity of 0.8 m/s (Mitchell, 1996). The rapid depositional growth will eventually lead to a sufficiently large diversity of terminal velocities and particles sizes needed for collisions. Moreover, turbulent motions frequently observed in the MPL (e.g., Morrison et al., 2012) can be expected to further enhance the likelihood for particle collisions. Their unique shape allows them to stick to each other by mechanical entanglement of their branches (Connolly et al., 2012; Pruppacher & Klett, 2012, Section 14.7).

4.3.2. Discussion: On the Absence of Aggregation Close to the Melting Level

The question remains, why do we not observe major DWR increases due to particle aggregation close to the melting level in low-level MPCs? Figure 4 highlights that increases in DWR are indeed observed at the liquid base, when its temperature is between −2 and 0°C. Considering the 1.6–2.0K uncertainty of the temperature retrievals in the MPL, we cannot exclude that this signature is caused by melting particles. Even if melting particles are not responsible for the enhanced DWRs, the DWRs found close to 0°C in Figures 3 and 4 are still significantly smaller than those observed in previous studies in midlatitude clouds (Chase et al., 2018; Dias Neto et al., 2019; Ori et al., 2020; Tridon et al., 2019), and in deeper cloud systems in Ny-Ålesund as well (Appendix C).

In general, enhanced aggregation close to the melting level is thought to be caused by the thickening of a quasi-liquid layer on the snowflake surface (Fabry & Zawadzki, 1995; Fletcher, 1962; Slater & Michaelides, 2019). This quasi-liquid layer forms on any ice particle, whether being a single crystal, aggregate, or rimed particle, and it increases its aggregation efficiency by enhancing its sticking efficiency. In extreme scenarios, this can lead to the formation of snowflakes several centimeters in size (Lawson et al., 1998). The absence of this second enhanced aggregation zone could be related to lower ice number concentrations in low-level MPCs at temperatures warmer than −10°C, compared to MPCs at dendritic-growth temperatures. However, the studies by Rangno and Hobbs (2001) and Mioche et al. (2017) have shown otherwise. They reported, based on airborne in-situ observations, that MPC events with CTT between −10 and 0°C, and MPC events with CTT between −20 and −10°C display similar ice number concentrations. Furthermore, signatures of secondary ice processes have been observed in Arctic MPCs close to the melting level (Luke et al., 2021).

Although we cannot provide a conclusive answer to this question with our remote sensing observations alone, we discuss possible processes that could lead to the observed lack of aggregation. First, the depositional growth rate at temperatures higher than −10°C is at least 1 order of magnitude smaller than at −15°C (see e.g., fig. 4 in Takahashi et al. (1991)). Due to the higher terminal fall velocities of columns, needles, and isometric particles, which are often observed in this temperature regime, the time for the particles to grow by deposition is also much shorter than in the DGZ. Due to this effect, particle populations that are fully nucleated at temperatures warmer than the DGZ might not develop broad enough size distributions to aggregate as efficiently as particles nucleated in or above the DGZ, despite the increase in sticking efficiency at temperatures higher than −5°C. Although we are not aware of evidence in literature to fully support this claim, Field et al. (2005) did report on average broader ice PSDs in the −5 to −15°C range, compared to the +5 to −5°C temperature interval, in midlatitude stratiform clouds, based on in-situ airborne observations. We thus hypothesize, that particle populations nucleated at temperatures compatible with dendritic-growth, or colder, are needed to trigger the typically observed enhanced aggregation close to the melting level. This is not the case in the low-level MPCs that are the focus of this study, as their limited depth often leads to CTT being warmer than −10°C when temperatures higher than −5°C are observed in the MPL.

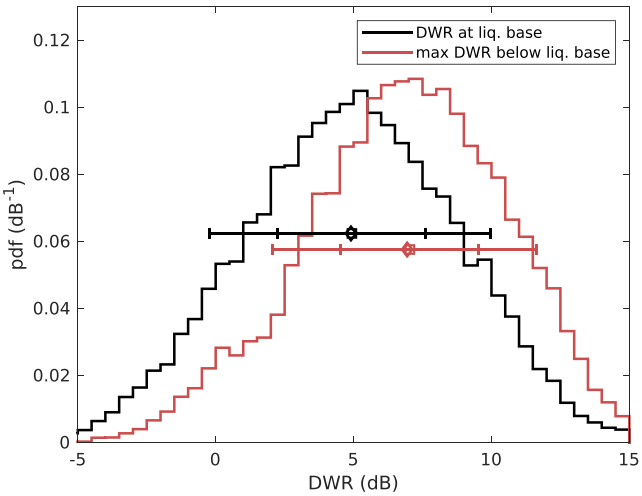

Figure 6. Probability density functions (PDFs) for dual-wavelength ratio (DWR) values at and below the liquid base in low-level mixed-phase clouds (MPCs). The black line is relative to values observed at liquid base, while the red line is relative to the maximum DWR value observed in each column below the liquid base. Error bars display 0.1, 0.25, 0.75, and 0.9 quantiles of the two distributions, with diamonds representing the mean values, and squares representing the median values. The data used are only for MPC events with liquid base temperature higher than −15°C and cloud-top temperature lower than −10°C. Samples with surface temperature warmer than 0°C are excluded. Bins are 0.5 dB wide.

A more frequent occurrence of riming, which was found in Kneifel and Moisseev (2020) to rapidly increase from −12°C toward 0°C, could further enhance the particles' terminal velocities and limit their residence time in the MPL. A suppression of aggregation by riming has been in fact suggested by Li et al. (2020), who observed lower DWRs (at X-band and Ka-band) in rimed snow, compared to unrimed snow, close to the melting level of stratiform precipitation events at Hyytiälä, Finland. Increased riming is likely in warmer MPC events at Ny-Ålesund, as remote sensing observations of single-layer MPCs at the site have shown a liquid fraction above 0.9 in more than 90% (80%) of the cases, when CTT is higher than −5°C (between −10 and −5°C) (Nomokonova, Ebell, et al., 2019). In contrast, liquid fractions for single-layer MPCs with CTTs between −15 and −10°C are below 0.8 in approximately 50% of the cases (Nomokonova, Ebell, et al., 2019). The dependence of DWR and MDV on LWP for MPCs in this temperature regime displayed in Figures 5e and 5f is also compatible with increased riming. DWR values are in fact close to 0 dB for LWP values larger than 15 g/m^2, and MDV values tend to increase with increasing LWP.

4.4. Further Aggregation Below the Mixed-Phase Layer

While the growth of dendritic branches from ice particles is likely to mostly take place in the mixed-phase layer of the MPC, as it requires high supersaturations with respect to ice (Pruppacher & Klett, 2012, Section 2.2), aggregation of ice particles can be expected to continue below it. Further increases in DWR below the MPL are in fact observed in the case study shown in Figure 1, for example, on February 4, 2021 between 7 and 11 UTC or between 22 and 24 UTC on the same day. In this section, we evaluate the further DWR increase below the MPL and how strong this increase is in relation to the aggregation signal at the liquid base. We restrict the analysis to profiles where the liquid-base temperatures are higher than −15°C and the CTTs are lower than −10°C as this is the region where we find the majority of large DWR signatures at liquid base. Connecting processes at different heights in one vertical profile is challenging, as the particles are advected by changing horizontal winds often causing complex fall streaks in the radar time-height display (Kalesse, Szyrmer, et al., 2016; Pfitzenmaier et al., 2017, 2018). To avoid these difficulties, we do not directly compare DWR values measured at different heights in the same column. Instead in Figure 6, we analyze the distributions of DWR values observed at the liquid base, and of the maximum DWR values observed below the liquid base in each column. Note that in a given column, these two values can be the same, if the maximum DWR is at liquid base: this is observed in 15.3% of the available samples. In order to avoid high DWR signals originating from melting particles, samples measured when surface temperature was warmer than 0°C are ignored in this analysis.

From Figure 6, it is clear that aggregation continues to increase mean aggregate size despite the likely sub-saturated air below liquid base (e.g., Shupe et al., 2008). The median (mean) of the largest DWRs observed below the MPL is 7.0 dB (6.9 dB), and is 43% (41%) larger than the median (mean) DWR of 4.9 dB (4.9 dB) at liquid base. Below the liquid base, we can attribute most of the DWR increase to aggregation, as riming cannot occur because of the absence of liquid water. The narrower distribution of the maximum DWR below liquid base is due to the fact that the DWRs approach the saturation value, as the particle sizes grow. DWR saturation values for unrimed and lightly rimed aggregates have been estimated in Appendix A to be 10–11 dB for the 24 and 94 GHz combination.

4.5. Persistence of High DWR Signals

Several previous studies demonstrated that Arctic MPCs display a complex horizontal structure, and high spatial variability in terms of dynamics and hydrometeors (Eirund et al., 2019; Ruiz-Donoso et al., 2020; Schäfer et al., 2018; Shupe et al., 2008). It appears therefore interesting to investigate whether the observed high DWR signatures are restricted to limited regions of the MPC, as observed in Figure 1, or whether enhanced aggregation tends to occur uniformly across the cloud field.

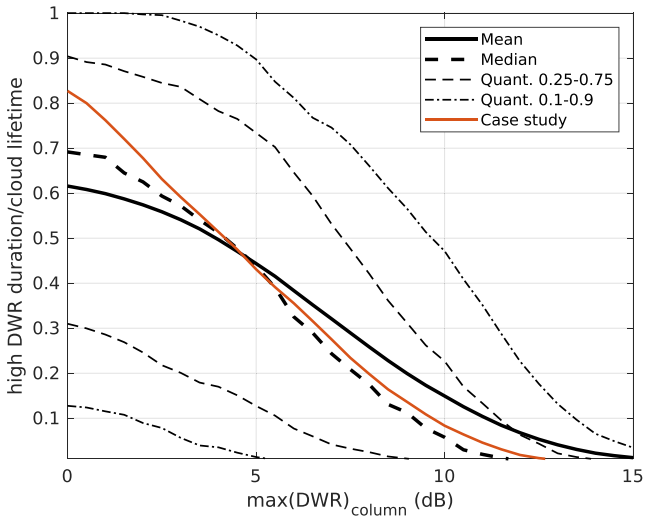

Figure 7. Distributions of the ratio between the duration of high dual-wavelength ratio (DWR) signals and the total duration of the mixed-phase cloud (MPC) event. The duration of high DWR signals is calculated as the total time during an MPC event that the maximum DWR in each column exceeds the value indicated on the *x*-axis. The curves indicate the mean, median, and quantiles of the duration ratio. Only MPC events with the mixed-phase layer at least partly at temperatures between −15 and −10°C are included. The red curve represents the case study observed on February 4–6, 2021, illustrated in Figure 1. Note that the quantity indicated on the *y*-axis, being a ratio between time intervals, is unitless.

The vertically pointing radars used in this study do not resolve the complete horizontal structure of the cloud field but rather observe the variability of clouds that are advected over the measurement site. The observed variability is thus usually a combination of temporal and spatial variability, and spatial variability is only resolved along the wind direction (e.g., Shupe et al., 2008). We estimated the duration of DWR signals exceeding certain thresholds and related them to the total duration of the MPC event (detected by the more sensitive W-band cloud radar, see Section 3). The full distribution of this quantity, together with its values for the case study in Figure 1, is shown in Figure 7. Note that, unlike the statistics presented in Sections 4.2–4.4, all available samples during MPC events were analyzed, including those with no signal in the MRR data. We would like to also highlight that the statistics shown in Figure 7 are sensitive to the definition of MPC event, as this in turn affects the event duration.

For interpreting Figure 7, it might help to consider first the red curve which represents the distribution of DWR in relation to the event duration from the case study shown in Figure 1. We see that cloud regions where the maximum DWR in each column exceeds 5 dB appear for 43.1% of the total MPC duration. Higher DWR values, for example, exceeding 8 dB, are only observed for 19.8% of the total duration of the event. The tendency of finding larger DWR values in shorter time periods of the cloud can also be observed when looking at the temporal DWR evolution shown in Figure 1c. High DWRs in the case study do not display a straightforward relation with features in the MDV (e.g., upward motions) or the reflectivity field.

Similarly to the case study, 50% of all MPC cases (median line) display DWR values larger than 5 dB for at least 43.8% of the event duration. For larger DWR thresholds, the quantile curves bend relatively quickly to decreasing duration ratios. Again, this result highlights that high DWR particles appear to form in limited regions of the cloud layer and for a limited amount of time, when compared to the cloud overall extent and duration. In summary, Figure 7 reveals that 50% of the observed MPCs display DWR values equal or higher than 2 (5, 8) dB for at least 62.5% (43.8%, 17.5%) of the total cloud duration. At the same time, 25% of the observed MPCs display DWR values equal or higher than 2 (5, 8) dB for at least 84.5% (70.2%, 36.1%) of the total cloud duration.

The analysis shown in the previous sections strongly suggests that temperatures compatible with the DGZ are essential in order for MPCs to produce large aggregates. However, their occurrence in limited regions of the MPC indicates that temperature might not be the only driver. Previous studies have shown that dynamical processes are essential in producing ice precipitation in Arctic MPCs, and that precipitation is in turn intertwined with the organization of the stratocumulus deck (Eirund et al., 2019; Shupe et al., 2008). At the same time, aerosol concentrations, surface conditions, and surface coupling significantly affect the phase partitioning (Gierens et al., 2020; Griesche et al., 2021; Kalesse, de Boer, et al., 2016; Norgren et al., 2018; Solomon et al., 2018). While we highlighted the relevance of the DGZ for the formation of large aggregates in low-level MPCs at Ny-Ålesund, investigating the role of individual processes for the formation of said aggregates is out of the scope of this study.

5. Conclusions and Open Questions

Using a combination of remote sensing instruments, in particular, a 24-GHz precipitation radar and a 94-GHz cloud radar, we evaluated the significance of different ice-growth processes, with a focus on aggregation, for the formation of precipitation in low-level MPCs at the high Arctic site of Ny-Ålesund. The combination of equivalent reflectivity factors measured at two radar frequencies into the DWR was used to obtain information on the characteristic size of the particle population. The 3-year statistics of DWR, matched with MDV, thermodynamic retrievals from a microwave radiometer, and phase information from the Cloudnet target classification, provided robust observational constraints for the microphysical processes leading to the formation of precipitation in low-level MPCs at the site.

This study revealed the unique role of the DGZ in the formation of precipitable ice particles in low-level MPCs at Ny-Ålesund, together with the absence of enhanced aggregation typically observed close to the melting level in deeper cloud systems. The main findings of this study are as follows:

1. Enhanced DWR signatures occurred predominantly in low-level MPCs whose mixed-phase layer was, at least partly, at temperatures between −15 and −10°C. This feature is compatible with similar signatures observed at the midlatitudes (Barrett et al., 2019; Dias Neto et al., 2019). This signature is typically attributed to enhanced aggregation due to mechanical entanglement of ice particles with dendritic branches, which preferentially grow in this temperature region (Pruppacher & Klett, 2012, Sections 2.2 and 14.7). In particular, the highest DWR values at the liquid base of the MPC were observed in conjunction with temperatures of −13 to −14°C, in agreement with laboratory studies that reported the highest depositional-growth rates at these temperatures (Takahashi, 2014; Takahashi et al., 1991). While riming likely also plays a role, as confirmed by increasing MDV with LWP, we argue that the growth of the larger ice particles is to be mainly attributed to rapid depositional growth of plate-like particles, and subsequent aggregation. Moreover, the relevance of aggregation in low-level MPCs in this temperature region is further confirmed by the additional increase in DWR observed below the liquid base, where riming cannot take place.
2. While our results demonstrate that mixed-phase layer temperatures compatible with dendritic growth are essential for the formation of large aggregates, these larger hydrometeors are only observed in limited regions of the cloud field. This suggests that dynamical processes might be at play in the formation of these larger aggregates. We reckon that further investigation is needed to understand the link between the growth of dendritic particles and their subsequent aggregation, and dynamics in low-level MPCs throughout the Arctic region.
3. Typically a second enhanced aggregation zone close to 0°C is observed in midlatitude clouds (Dias Neto et al., 2019; Fabry & Zawadzki, 1995), and in deeper cloud systems in Ny-Ålesund as well. This is usually attributed to the increased sticking efficiency of melting ice particles. The lack of high DWR signals close to the melting level (−5 to 0°C) in low-level MPCs in Ny-Ålesund suggests that this process is absent in these clouds. Since low-level MPCs span a limited temperature range, particles sedimenting from colder temperatures, characterized by a broader size distribution, might be necessary to trigger the enhanced aggregation typically observed. As such, further investigating this temperature regime bears the potential to substantially improve our understanding of aggregation in general, not only limited to low-level MPCs. While we cannot provide a conclusive answer from the remote-sensing perspective, we speculate that specific ice habits and increased riming might contribute to the suppression of aggregation. Ice habits that grow at temperatures higher than −10°C typically have faster fall velocities and smaller cross sections than dendrites (Kajikawa, 1972; Mitchell, 1996; Pruppacher & Klett, 2012, Sections 2.2, 10.5). Additionally, lower depositional growth rates have been reported at temperatures warmer than −10°C, compared to dendritic-growth temperatures (Takahashi et al., 1991). MDV information, together with evidence of increased drizzle production and riming reported in previous studies (Cortinas Jr et al., 2004; Kneifel & Moisseev, 2020; Nomokonova, Ebell, et al., 2019; Zhang et al., 2017), indicates that riming might also be relevant at these temperatures, and might suppress aggregation.

While it is reasonable to assume that similar microphysical processes occur in low-level MPCs throughout the whole Arctic region, because of the homogeneous characteristics that they display across different sites (de Boer et al., 2009; Gierens et al., 2020; Morrison et al., 2012; Nomokonova, Ebell, et al., 2019; Shupe, 2011; Shupe et al., 2006; Zhao & Wang, 2010), this hypothesis should be tested by looking for similar observational fingerprints at other Arctic observatories. The multi-frequency and Doppler radar observations presented in this study provided strong observational constraints for the microphysical processes taking place in low-level MPCs at Ny-Ålesund, nevertheless the range of observational fingerprints can be substantially extended with polarimetric observations. The recent extension of the AWIPEV site with a polarimetric Ka-band radar will allow us to better constrain ice particle concentration and shape in the future. It will further enable us to obtain DWR profiles reaching cloud top, as well as overcome the sensitivity limitations of the MRR. In this regard, dual-frequency cloud radar observations provide the unique opportunity to test and improve the representation of ice-growth processes in numerical models (Karrer et al., 2021; Ori et al., 2020), and this possibility will be in the future explored with the ICOsahedral Non-hydrostatic (ICON) modeling framework (Zängl et al., 2015), in its Large Eddy Model (LEM) version.

Appendix A: Examples of DWR Dependence on Particle Size

Figure A1 illustrates examples of DWR dependence on ice particle shape and size. DWR values were computed using the scattering database developed by Ori et al. (2021). PSDs are assumed to be inverse exponential, and the figure shows the dependency of DWR on the mass median diameter $D0$. The chosen particle types are: unrimed dendrite aggregates, unrimed column and dendrite aggregates, and rimed column and dendrite aggregates. Three values for the degree of riming have been chosen, indicated by the effective LWP (ELWP): 0.1, 0.2, and 0.5 kg/m^2. ELWP is defined as the LWP that produces the simulated amount of riming, assuming a riming efficiency of 100% (Leinonen et al., 2018; Leinonen & Szyrmer, 2015). The figure shows that DWR is 0 dB when $D0$ is 1 mm for all particle types, it then rapidly increases as $D0$ increases. It then reaches a saturation value between 10 and 11 dB for unrimed and lightly rimed (ELWP = 0.1, 0.2 kg/m^2) aggregates, when $D0$ is above 10 mm. The saturation value is higher for higher degrees of riming.

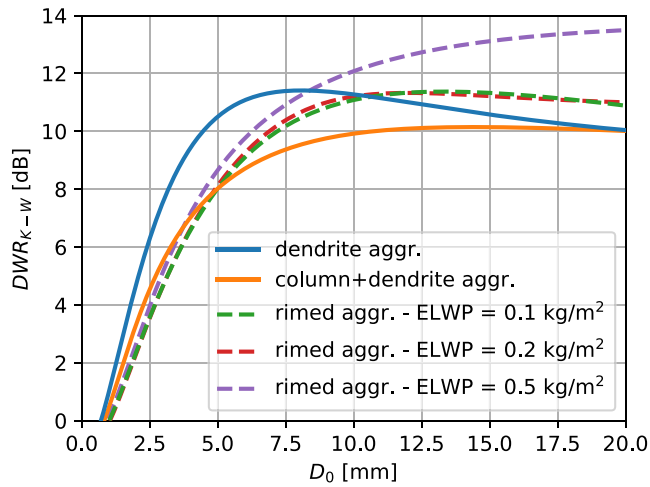

Figure A1. Calculation of dual-wavelength ratio (DWR) at K-band (24.2 GHz) and W-band (94.0 GHz) for different ice particle types, as function of the mass median diameter $D0$, obtained with the scattering database by Ori et al. (2021). The ice particles included are: unrimed dendrite aggregates, unrimed dendrite and column aggregates, and rimed dendrite and column aggregates. The degree of riming for the rimed aggregates is indicated by the effective liquid water path (ELWP, see text for definition).

Appendix B: Example of the Calibration Procedure and List of Derived Calibration Offsets

Figure B1 shows an example of the calibration procedure described in Section 3.2.1. The figure depicts a monthly histogram of DWR for the month of December 2020, before (a) and after (b) applying the calibration procedure. Only data observed during calibration events (see Section 3.2.1) are included. The calibration procedure consists in determining the mode of the uncalibrated DWR histogram (vertical line in panel a), which is then used as monthly offset for the W-band reflectivities. This approach thus relies on the assumption that the peak of the distribution is associated with Rayleigh scattering, and the tail on the right side of the peak is associated with non-Rayleigh scattering. The offset is then added to all W-band reflectivities, leading to the whole histogram being shifted so that its mode is now at 0 dB (panel b, dashed vertical line). The uncertainty on DWR is calculated by assuming that all DWR values on the left side of the peak are associated with Rayleigh scattering. The left-side standard deviation (i.e., only for calibrated DWR values lower than 0 dB) with respect to the mode is thus taken as uncertainty (dash-dotted line in panel b).

All derived monthly offsets for all radar systems are displayed in Table B1.

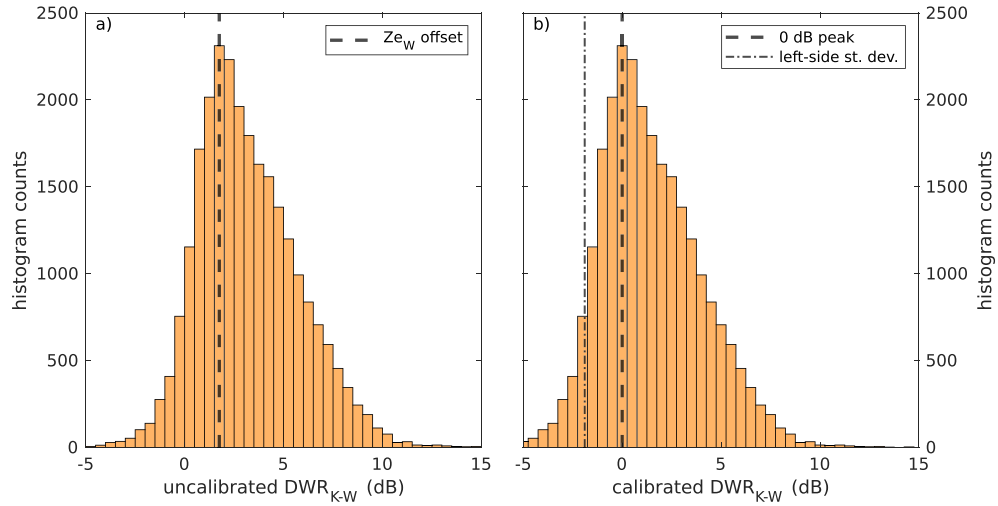

Figure B1. Monthly dual-wavelength ratio (DWR) histograms for the month of December 2020 before (panel a) and after (panel b) applying the calibration procedure. Only DWR values observed during calibration events are included in the histogram. The dashed vertical lines in panels (a) and (b) indicate the mode of the distribution, while the dash-dotted vertical line in panel (b) indicates the left-side standard deviation with respect to the mode. See text for more details. Bins in both histograms are 0.5 dB wide.

Table B1
Monthly Calibration Offsets Obtained for the Three Radar Systems Used in the Study, Expressed in dB

Month	09/2017	10/2017	11/2017	12/2017	01/2018	02/2018	03/2018	04/2018	05/2018	06/2018	07/2018	08/2018	09/2018	10/2018
MRR-2	−0.81	(−0.87)	(−0.92)	(−0.98)	(−1.04)	(−1.10)	(−1.15)	(−1.21)	(−1.27)	−1.33	−1.33	−1.33	−1.33	(−1.35)
MiRAC-A	−0.75	2.75	3.25	3.75	2.25	4.75	2.25	2.75	2.75	1.25	0.75	0.75	1.25	2.75
Month	06/2019	07/2019	08/2019	09/2019	10/2019	11/2019	12/2019	01/2020	02/2020	03/2020	04/2020	05/2020	06/2020	07/2020
MRR-2	−1.57	−1.57	−1.57	−1.57	(−1.61)	(−1.64)	(−1.68)	(−1.71)	(−1.74)	(−1.78)	(−1.81)	(−1.85)	−1.88	−1.88
JOYRAD-94	1.75	−0.25	−0.25	−0.25	0.75	1.25	2.25	2.25	1.75	0.75	0.75	5.25	0.25	−0.25
Month	08/2020	09/2020	10/2020	11/2020	12/2020	01/2021	02/2021	–	06–09/2021					
MRR-2	−1.88	−1.88	(−1.88)	(−1.89)	(−1.89)	(−1.89)	(−1.90)	–	−1.91					
JOYRAD-94	−0.25	1.25	−0.25	3.25	1.75	1.25	1.25	–	–					

Note. Values indicated in parentheses were obtained by linear interpolation.

Appendix C: DWR Signatures in Deep Cloud Systems in Ny-Ålesund

Similarly to Figure 3, Figure C1 displays CFTDs of DWR and MDV. All cloud systems with cloud-top height higher than 2.5 km detected during the study period were included in this figure, adding up to a total duration of 2,941 hr. DWR and MDV values are matched with temperature (T) retrieved at the same height, and the figure displays joint histograms of DWR and T (panel a), and MDV and T (panel b).

In addition to the typical increase in DWR corresponding to the DGZ (Barrett et al., 2019; Dias Neto et al., 2019; Lamer et al., 2021; Ori et al., 2020; Oue et al., 2021), the figure displays a further increase in DWR close to the melting level, which is typically observed at the midlatitudes (Chase et al., 2018; Dias Neto et al., 2019; Ori et al., 2020; Tridon et al., 2019).

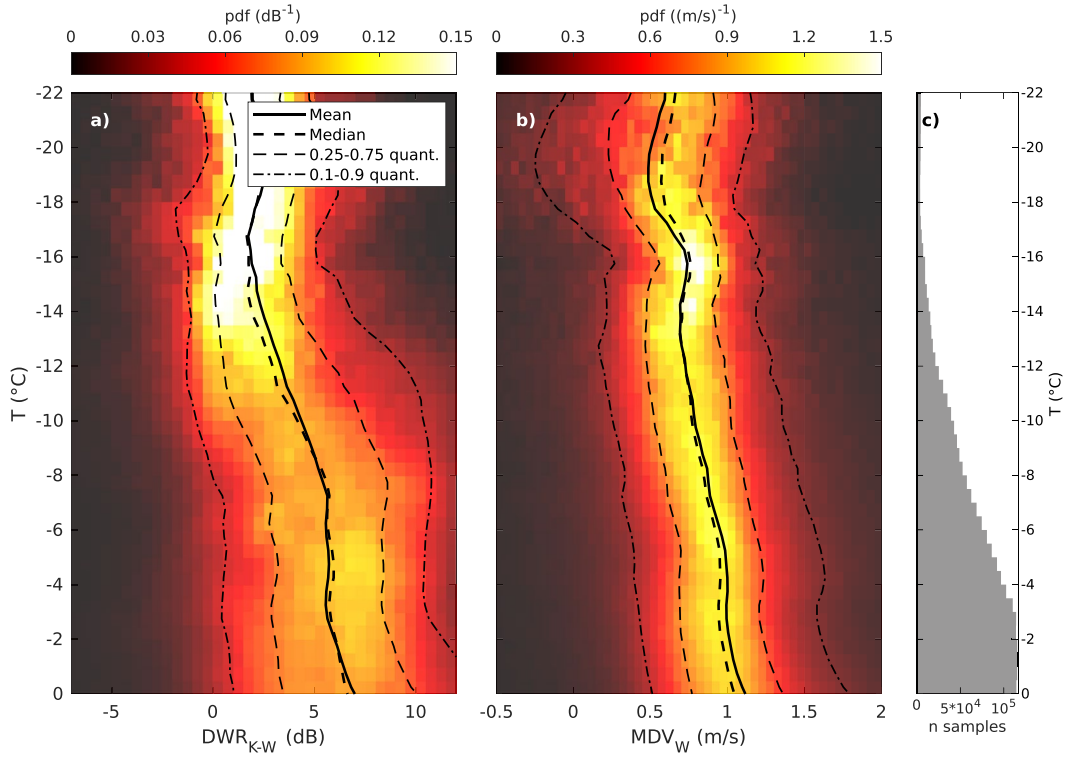

Figure C1. Contoured frequency by temperature diagram (CFTD) of dual-wavelength ratio (DWR) and mean Doppler velocity (MDV) in clouds with cloud-top height above 2.5 km. All clouds with cloud-top height above 2.5 km that are detected by the Micro Rain Radar (MRR) during the study period at sub-zero temperatures are included. Panel (c) displays the number of samples available at each temperature level. Since MDV is obtained from the W-band cloud radar, MDV values are only included if MRR echoes are available. Bin sizes are: 1 dB, 0.05 m/s, 0.5°C.

Data Availability Statement

Microwave radiometer retrievals are available in Nomokonova, Ritter, and Ebell (2019) (for the 2017–2018 period), and in Ebell and Ritter (2022) (for the 2019–2021 period). The Cloudnet target classification product can be downloaded from https://cloudnet.fmi.fi/. The processed DWR and MDV data are available in Chellini et al. (2022). Although not necessary to reproduce the results reported in this study, the MRR and 94-GHz cloud radar original data will be published in the near future on the PANGAEA archive (https://pangaea.de).

References

Abel, S. J., Boutle, I. A., Waite, K., Fox, S., Brown, P. R., Cotton, R., et al. (2017). The role of precipitation in controlling the transition from stratocumulus to cumulus clouds in a Northern Hemisphere cold-air outbreak. *Journal of the Atmospheric Sciences*, *74*(7), 2293–2314. https://doi.org/10.1175/JAS-D-16-0362.1

Avramov, A., Ackerman, A. S., Fridlind, A. M., van Diedenhoven, B., Botta, G., Aydin, K., et al. (2011). Toward ice formation closure in Arctic mixed-phase boundary layer clouds during ISDAC. *Journal of Geophysical Research: Atmospheres*, *116*(D1), D00T08. https://doi.org/10.1029/2011JD015910

Avramov, A., & Harrington, J. Y. (2010). Influence of parameterized ice habit on simulated mixed phase Arctic clouds. *Journal of Geophysical Research: Atmospheres*, *115*(D3), D03205. https://doi.org/10.1029/2009JD012108

Bailey, M. P., & Hallett, J. (2009). A comprehensive habit diagram for atmospheric ice crystals: Confirmation from the laboratory, AIRS II, and other field studies. *Journal of the Atmospheric Sciences*, *66*(9), 2888–2899. https://doi.org/10.1175/2009JAS2883.1

Barrett, A. I., Westbrook, C. D., Nicol, J. C., & Stein, T. H. M. (2019). Rapid ice aggregation process revealed through triple-wavelength Doppler spectrum radar analysis. *Atmospheric Chemistry and Physics*, *19*(8), 5753–5769. https://doi.org/10.5194/acp-19-5753-2019

Barthazy, E., & Schefold, R. (2006). Fall velocity of snowflakes of different riming degree and crystal types. *Atmospheric Research*, *82*(1–2), 391–398. https://doi.org/10.1016/j.atmosres.2005.12.009

Battaglia, A., Rustemeier, E., Tokay, A., Blahak, U., & Simmer, C. (2010). PARSIVEL snow observations: A critical assessment. *Journal of Atmospheric and Oceanic Technology*, *27*(2), 333–344. https://doi.org/10.1175/2009JTECHA1332.1

Battaglia, A., Tanelli, S., Tridon, F., Kneifel, S., Leinonen, J., & Kollias, P. (2020). Triple-frequency radar retrievals. In V. Levizzani, C. Kidd, D. B. Kirschbaum, C. D. Kummerow, K. Nakamura, & F. J. Turk (Eds.), *Satellite precipitation measurement* (Vol. 1, pp. 211–229). Springer International Publishing. https://doi.org/10.1007/978-3-030-24568-9_13

Acknowledgments
The authors gratefully acknowledge the funding by the Deutsche Forschungsgemeinschaft (DFG, German Research Foundation)—Project no. 268020496—TRR 172, within the Transregional Collaborative Research Center "ArctiC Amplification: Climate Relevant Atmospheric and SurfaCe Processes, and Feedback Mechanisms (AC)^3." Contributions by Stefan Kneifel were funded by the DFG under grant KN 1112/2-1 and KN 1112/2-2 as part of the Emmy-Noether Group "Optimal combination of Polarimetric and Triple Frequency radar techniques for Improving Microphysical process understanding of cold clouds" (OPTIMice). This study would not have been possible without Kerstin Ebell and Pavel Krobot, who managed the data, including the application of the Cloudnet algorithm. In this regard, the authors would also like to thank the Alfred Wegener Institute (AWI) for sharing their HATPRO and ceilometer data. The authors wish to thank Lukas Pfitzenmaier, whose assistance was invaluable when evaluating the calibration of the radar systems, and Davide Ori, for producing the scattering tables used in the disdrometer-based calibration. The authors would like to further acknowledge the discussions with Ulrich Löhnert and Maximilian Maahn, which helped improve the manuscript. Last but not least, the authors wish to thank the AWIPEV staff for operating the instruments. The authors would like to express their gratitude to the three anonymous reviewers, whose constructive criticism helped significantly improve the quality of the manuscript. GC also acknowledges the support from the Graduate School of Geosciences (GSGS) of the University of Cologne, as well as the Integrated Research Training Group (IRTG) of the (AC)^3 consortium. Open Access funding enabled and organized by Projekt DEAL.

Brandes, E. A., Ikeda, K., Thompson, G., & Schönhuber, M. (2008). Aggregate terminal velocity/temperature relations. *Journal of Applied Meteorology and Climatology*, *47*(10), 2729–2736. https://doi.org/10.1175/2008JAMC1869.1

Cha, J.-W., Chang, K.-H., Yum, S. S., & Choi, Y.-J. (2009). Comparison of the bright band characteristics measured by Micro Rain Radar (MRR) at a mountain and a coastal site in South Korea. *Advances in Atmospheric Sciences*, *26*(2), 211–221. https://doi.org/10.1007/s00376-009-0211-0

Chase, R. J., Finlon, J. A., Borque, P., McFarquhar, G. M., Nesbitt, S. W., Tanelli, S., et al. (2018). Evaluation of triple-frequency radar retrieval of snowfall properties using coincident airborne in situ observations during OLYMPEX. *Geophysical Research Letters*, *45*(11), 5752–5760. https://doi.org/10.1029/2018GL077997

Chellini, G., Gierens, R., & Kneifel, S. (2022). Dual-wavelength radar observations of precipitation at Ny-Ålesund (1 Sep. 2017 - 9 Oct. 2018, 14 June 2019 - 28 Feb. 2021). [Dataset]. PANGAEA. https://doi.pangaea.de/10.1594/PANGAEA.943550

Connolly, P., Emersic, C., & Field, P. (2012). A laboratory investigation into the aggregation efficiency of small ice crystals. *Atmospheric Chemistry and Physics*, *12*(4), 2055–2076. https://doi.org/10.5194/acp-12-2055-2012

Cortinas, J. V., Jr., Bernstein, B. C., Robbins, C. C., & Walter Strapp, J. (2004). An analysis of freezing rain, freezing drizzle, and ice pellets across the United States and Canada: 1976–90. *Weather and Forecasting*, *19*(2), 377–390. https://doi.org/10.1175/1520-0434(2004)019<0377:aaofrf>2.0.co;2

Crewell, S., & Lohnert, U. (2007). Accuracy of boundary layer temperature profiles retrieved with multifrequency multiangle microwave radiometry. *IEEE Transactions on Geoscience and Remote Sensing*, *45*(7), 2195–2201. https://doi.org/10.1109/TGRS.2006.888434

Dahlke, S., & Maturilli, M. (2017). Contribution of atmospheric advection to the amplified winter warming in the Arctic North Atlantic region. *Advances in Meteorology*, *2017*, 4928620. https://doi.org/10.1155/2017/4928620

de Boer, G., Eloranta, E. W., & Shupe, M. D. (2009). Arctic mixed-phase stratiform cloud properties from multiple years of surface-based measurements at two high-latitude locations. *Journal of the Atmospheric Sciences*, *66*(9), 2874–2887. https://doi.org/10.1175/2009JAS3029.1

Dias Neto, J., Kneifel, S., Ori, D., Trömel, S., Handwerker, J., Bohn, B., et al. (2019). The TRIple-frequency and Polarimetric radar Experiment for improving process observations of winter precipitation. *Earth System Science Data*, *11*(2), 845–863. https://doi.org/10.5194/essd-11-845-2019

Durán-Alarcón, C., Boudevillain, B., Genthon, C., Grazioli, J., Souverijns, N., van Lipzig, N. P., et al. (2019). The vertical structure of precipitation at two stations in East Antarctica derived from micro rain radars. *The Cryosphere*, *13*(1), 247–264. https://doi.org/10.5194/tc-13-247-2019

Ebell, K., Nomokonova, T., Maturilli, M., & Ritter, C. (2020). Radiative effect of clouds at Ny-Ålesund, Svalbard, as inferred from ground-based remote sensing observations. *Journal of Applied Meteorology and Climatology*, *59*(1), 3–22. https://doi.org/10.1175/JAMC-D-19-0080.1

Ebell, K., & Ritter, C. (2022). HATPRO microwave radiometer measurements at AWIPEV, Ny-Ålesund (2019-2021). [Dataset]. PANGAEA. https://doi.pangaea.de/10.1594/PANGAEA.943004

Eirund, G. K., Lohmann, U., & Possner, A. (2019). Cloud ice processes enhance spatial scales of organization in Arctic stratocumulus. *Geophysical Research Letters*, *46*(23), 14109–14117. https://doi.org/10.1029/2019GL084959

Fabry, F. (2018). *Radar meteorology: Principles and practice*. Cambridge University Press. https://doi.org/10.1017/CBO9781107707405

Fabry, F., & Zawadzki, I. (1995). Long-term radar observations of the melting layer of precipitation and their interpretation. *Journal of the Atmospheric Sciences*, *52*(7), 838–851. https://doi.org/10.1175/1520-0469(1995)052<0838:ltroot>2.0.co;2

Field, P., Hogan, R., Brown, P., Illingworth, A., Choularton, T., & Cotton, R. (2005). Parametrization of ice-particle size distributions for mid-latitude stratiform cloud. *Quarterly Journal of the Royal Meteorological Society: A Journal of the Atmospheric Sciences, Applied Meteorology and Physical Oceanography*, *131*(609), 1997–2017. https://doi.org/10.1256/qj.04.134

Fitch, K. E., & Garrett, T. J. (2022). Graupel precipitating from thin arctic clouds with liquid water paths less than 50 g m^{-2}. *Geophysical Research Letters*, *49*(1), e2021GL094075. https://doi.org/10.1029/2021GL094075

Fletcher, N. H. (1962). Surface structure of water and ice. *Philosophical Magazine*, *7*(74), 255–269. https://doi.org/10.1080/14786436208211860

Gierens, R. (2021). Observations of Arctic low-level mixed-phase clouds at Ny-Ålesund: Characterization and insights gained by high-resolution Doppler radar. (Doctoral dissertation, Universität zu Köln, Köln). Retrieved from https://kups.ub.uni-koeln.de/53900/

Gierens, R., Kneifel, S., Shupe, M. D., Ebell, K., Maturilli, M., & Löhnert, U. (2020). Low-level mixed-phase clouds in a complex Arctic environment. *Atmospheric Chemistry and Physics*, *20*(6), 3459–3481. https://doi.org/10.5194/acp-20-3459-2020

Grazioli, J., Madeleine, J.-B., Gallée, H., Forbes, R. M., Genthon, C., Krinner, G., & Berne, A. (2017). Katabatic winds diminish precipitation contribution to the Antarctic ice mass balance. *Proceedings of the National Academy of Sciences of the United States of America*, *114*(41), 10858–10863. https://doi.org/10.1073/pnas.1707633114

Griesche, H. J., Ohneiser, K., Seifert, P., Radenz, M., Engelmann, R., & Ansmann, A. (2021). Contrasting ice formation in arctic clouds: Surface-coupled vs. surface-decoupled clouds. *Atmospheric Chemistry and Physics*, *21*(13), 10357–10374. https://doi.org/10.5194/acp-21-10357-2021

Harrington, J. Y., & Olsson, P. Q. (2001). On the potential influence of ice nuclei on surface-forced marine stratocumulus cloud dynamics. *Journal of Geophysical Research: Atmospheres*, *106*(D21), 27473–27484. https://doi.org/10.1029/2000JD000236

Heymsfield, A. J., Van Zadelhoff, G.-J., Donovan, D. P., Fabry, F., Hogan, R. J., & Illingworth, A. J. (2007). Refinements to ice particle mass dimensional and terminal velocity relationships for ice clouds. Part II: Evaluation and parameterizations of ensemble ice particle sedimentation velocities. *Journal of the Atmospheric Sciences*, *64*(4), 1068–1088. https://doi.org/10.1175/JAS3900.1

Heymsfield, A. J., & Westbrook, C. (2010). Advances in the estimation of ice particle fall speeds using laboratory and field measurements. *Journal of the Atmospheric Sciences*, *67*(8), 2469–2482. https://doi.org/10.1175/2010JAS3379.1

Hogan, R. J., Illingworth, A. J., & Sauvageot, H. (2000). Measuring crystal size in cirrus using 35-and 94-GHz radars. *Journal of Atmospheric and Oceanic Technology*, *17*(1), 27–37. https://doi.org/10.1175/1520-0426(2000)017<0027:mcsicu>2.0.co;2

Hogan, R. J., & O'Connor, E. J. (2004). Facilitating cloud radar and lidar algorithms: The cloudnet instrument synergy/target categorization product. Cloudnet documentation, 14.

Huang, G.-J., Bringi, V. N., & Thurai, M. (2008). Orientation angle distributions of drops after an 80-m fall using a 2D video disdrometer. *Journal of Atmospheric and Oceanic Technology*, *25*(9), 1717–1723. https://doi.org/10.1175/2008JTECHA1075.1

Illingworth, A., Hogan, R., O'connor, E., Bouniol, D., Brooks, M., Delanoë, J., et al. (2007). CLOUDNET: Continuous evaluation of cloud profiles in seven operational models using ground-based observations. *Bulletin of the American Meteorological Society*, *88*(6), 883–898. https://doi.org/10.1175/bams-88-6-883

Jackson, R. C., McFarquhar, G. M., Korolev, A. V., Earle, M. E., Liu, P. S., Lawson, R. P., et al. (2012). The dependence of ice microphysics on aerosol concentration in arctic mixed-phase stratus clouds during ISDAC and M-PACE. *Journal of Geophysical Research: Atmospheres*, *117*(D15), D15207. https://doi.org/10.1029/2012JD017668

Kajikawa, M. (1972). Measurement of falling velocity of individual snow crystals. *Journal of the Meteorological Society of Japan Ser. II*, *50*(6), 577–584. https://doi.org/10.2151/jmsj1965.50.6_577

Kalesse, H., de Boer, G., Solomon, A., Oue, M., Ahlgrimm, M., Zhang, D., et al. (2016). Understanding rapid changes in phase partitioning between cloud liquid and ice in stratiform mixed-phase clouds: An arctic case study. *Monthly Weather Review*, *144*(12), 4805–4826. https://doi.org/10.1175/MWR-D-16-0155.1

Kalesse, H., Szyrmer, W., Kneifel, S., Kollias, P., & Luke, E. (2016). Fingerprints of a riming event on cloud radar Doppler spectra: Observations and modeling. *Atmospheric Chemistry and Physics*, *16*(5), 2997–3012. https://doi.org/10.5194/acp-16-2997-2016

Karrer, M., Seifert, A., Ori, D., & Kneifel, S. (2021). Improving the representation of aggregation in a two-moment microphysical scheme with statistics of multi-frequency Doppler radar observations. *Atmospheric Chemistry and Physics*, *21*(22), 17133–17166. https://doi.org/10.5194/acp-21-17133-2021

Karrer, M., Seifert, A., Siewert, C., Ori, D., von Lerber, A., & Kneifel, S. (2020). Ice particle properties inferred from aggregation modelling. *Journal of Advances in Modeling Earth Systems*, *12*(8), e2020MS002066. https://doi.org/10.1029/2020MS002066

Klugmann, D., Heinsohn, K., & Kirtzel, H. J. (1996). A low cost 24 GHz FM-CW Doppler radar rain profiler. *Contributions to Atmospheric Physics*, *69*.

Kneifel, S., Kollias, P., Battaglia, A., Leinonen, J., Maahn, M., Kalesse, H., & Tridon, F. (2016). First observations of triple-frequency radar Doppler spectra in snowfall: Interpretation and applications. *Geophysical Research Letters*, *43*(5), 2225–2233. https://doi.org/10.1002/2015GL067618

Kneifel, S., Maahn, M., Peters, G., & Simmer, C. (2011). Observation of snowfall with a low-power FM-CW K-band radar (Micro Rain Radar). *Meteorology and Atmospheric Physics*, *113*(1), 75–87. https://doi.org/10.1007/s00703-011-0142-z

Kneifel, S., & Moisseev, D. (2020). Long-term statistics of riming in nonconvective clouds derived from ground-based Doppler cloud radar observations. *Journal of the Atmospheric Sciences*, *77*(10), 3495–3508. https://doi.org/10.1175/JAS-D-20-0007.1

Kobayashi, T. (1957). Experimental researches en the snow crystal habit and growth by means of a diffusion cloud chamber. *Journal of the Meteorological Society of Japan Ser. II*, *35*, 38–47. https://doi.org/10.2151/jmsj1923.35A.0_38

Korolev, A. (2007). Limitations of the Wegener–Bergeron–Findeisen mechanism in the evolution of mixed-phase clouds. *Journal of the Atmospheric Sciences*, *64*(9), 3372–3375. https://doi.org/10.1175/JAS4035.1

Korolev, A., & Mazin, I. P. (2003). Supersaturation of water vapor in clouds. *Journal of the Atmospheric Sciences*, *60*(24), 2957–2974. https://doi.org/10.1175/1520-0469(2003)060<2957:sowvic>2.0.co;2

Küchler, N., Kneifel, S., Löhnert, U., Kollias, P., Czekala, H., & Rose, T. (2017). A W-band radar–radiometer system for accurate and continuous monitoring of clouds and precipitation. *Journal of Atmospheric and Oceanic Technology*, *34*(11), 2375–2392. https://doi.org/10.1175/JTECH-D-17-0019.1

Lamer, K., Oue, M., Battaglia, A., Roy, R. J., Cooper, K. B., Dhillon, R., & Kollias, P. (2021). Multifrequency radar observations of clouds and precipitation including the G-band. *Atmospheric Measurement Techniques*, *14*(5), 3615–3629. https://doi.org/10.5194/amt-14-3615-2021

Lawson, R. P., Stewart, R. E., & Angus, L. J. (1998). Observations and numerical simulations of the origin and development of very large snowflakes. *Journal of the Atmospheric Sciences*, *55*(21), 3209–3229. https://doi.org/10.1175/1520-0469(1998)055<3209:oansot>2.0.co;2

Leinonen, J. (2014). High-level interface to T-matrix scattering calculations: Architecture, capabilities and limitations. *Optics Express*, *22*(2), 1655–1660. https://doi.org/10.1364/OE.22.001655

Leinonen, J., Kneifel, S., & Hogan, R. J. (2018). Evaluation of the Rayleigh–Gans approximation for microwave scattering by rimed snowflakes. *Quarterly Journal of the Royal Meteorological Society*, *144*(S1), 77–88. https://doi.org/10.1002/qj.3093

Leinonen, J., & Szyrmer, W. (2015). Radar signatures of snowflake riming: A modeling study. *Earth and Space Science*, *2*(8), 346–358. https://doi.org/10.1002/2015EA000102

Li, H., Tiira, J., von Lerber, A., & Moisseev, D. (2020). Towards the connection between snow microphysics and melting layer: Insights from multifrequency and dual-polarization radar observations during BAECC. *Atmospheric Chemistry and Physics*, *20*(15), 9547–9562. https://doi.org/10.5194/acp-20-9547-2020

Liao, L., Meneghini, R., Iguchi, T., & Detwiler, A. (2005). Use of dual-wavelength radar for snow parameter estimates. *Journal of Atmospheric and Oceanic Technology*, *22*(10), 1494–1506. https://doi.org/10.1175/JTECH1808.1

Locatelli, J. D., & Hobbs, P. V. (1974). Fall speeds and masses of solid precipitation particles. *Journal of Geophysical Research*, *79*(15), 2185–2197. https://doi.org/10.1029/JC079i015p02185

Löffler-Mang, M., & Joss, J. (2000). An optical disdrometer for measuring size and velocity of hydrometeors. *Journal of Atmospheric and Oceanic Technology*, *17*(2), 130–139. https://doi.org/10.1175/1520-0426(2000)017⟨0130:AODFMS⟩2.0.CO;2

Luke, E. P., Yang, F., Kollias, P., Vogelmann, A. M., & Maahn, M. (2021). New insights into ice multiplication using remote-sensing observations of slightly supercooled mixed-phase clouds in the Arctic. *Proceedings of the National Academy of Sciences of the United States of America*, *118*(13), e2021387118. https://doi.org/10.1073/pnas.2021387118

Maahn, M., Burgard, C., Crewell, S., Gorodetskaya, I. V., Kneifel, S., Lhermitte, S., et al. (2014). How does the spaceborne radar blind zone affect derived surface snowfall statistics in polar regions? *Journal of Geophysical Research: Atmospheres*, *119*(24), 13–604. https://doi.org/10.1002/2014JD022079

Maahn, M., & Kollias, P. (2012). Improved Micro Rain Radar snow measurements using Doppler spectra post-processing. *Atmospheric Measurement Techniques*, *5*(11), 2661–2673. https://doi.org/10.5194/amt-5-2661-2012

Mason, S. L., Hogan, R. J., Westbrook, C. D., Kneifel, S., Moisseev, D., & von Terzi, L. (2019). The importance of particle size distribution and internal structure for triple-frequency radar retrievals of the morphology of snow. *Atmospheric Measurement Techniques*, *12*(9), 4993–5018. https://doi.org/10.5194/amt-12-4993-2019

Matrosov, S. Y., Heymsfield, A., & Wang, Z. (2005). Dual-frequency radar ratio of nonspherical atmospheric hydrometeors. *Geophysical Research Letters*, *32*(13), L13816. https://doi.org/10.1029/2005GL023210

Matrosov, S. Y., Maahn, M., & De Boer, G. (2019). Observational and modeling study of ice hydrometeor radar dual-wavelength ratios. *Journal of Applied Meteorology and Climatology*, *58*(9), 2005–2017. https://doi.org/10.1175/JAMC-D-19-0018.1

Maturilli, M., & Ebell, K. (2018). Twenty-five years of cloud base height measurements by ceilometer in Ny-Ålesund, Svalbard. *Earth System Science Data*, *10*(3), 1451–1456. https://doi.org/10.5194/essd-10-1451-2018

Maturilli, M., Herber, A., & König-Langlo, G. (2013). Climatology and time series of surface meteorology in Ny-Ålesund, Svalbard. *Earth System Science Data*, *5*(1), 155–163. https://doi.org/10.5194/essd-5-155-2013

Maturilli, M., & Kayser, M. (2017). Arctic warming, moisture increase and circulation changes observed in the Ny-Ålesund homogenized radiosonde record. *Theoretical and Applied Climatology*, *130*(1), 1–17. https://doi.org/10.1007/s00704-016-1864-0

Matus, A. V., & L'Ecuyer, T. S. (2017). The role of cloud phase in Earth's radiation budget. *Journal of Geophysical Research: Atmospheres*, *122*(5), 2559–2578. https://doi.org/10.1002/2016JD025951

McFarquhar, G. M., Zhang, G., Poellot, M. R., Kok, G. L., McCoy, R., Tooman, T., et al. (2007). Ice properties of single-layer stratocumulus during the Mixed-Phase Arctic Cloud Experiment: 1. Observations. *Journal of Geophysical Research: Atmospheres*, *112*(D24), D24201. https://doi.org/10.1029/2007JD008633

Mech, M., Kliesch, L.-L., Anhäuser, A., Rose, T., Kollias, P., & Crewell, S. (2019). Microwave Radar/radiometer for Arctic Clouds (MiRAC): First insights from the ACLOUD campaign. *Atmospheric Measurement Techniques*, *12*(9), 5019–5037. https://doi.org/10.5194/amt-12-5019-2019

Mioche, G., Jourdan, O., Ceccaldi, M., & Delanoë, J. (2015). Variability of mixed-phase clouds in the Arctic with a focus on the Svalbard region: A study based on spaceborne active remote sensing. *Atmospheric Chemistry and Physics*, *15*(5), 2445–2461. https://doi.org/10.5194/acp-15-2445-2015

Mioche, G., Jourdan, O., Delanoë, J., Gourbeyre, C., Febvre, G., Dupuy, R., et al. (2017). Vertical distribution of microphysical properties of Arctic springtime low-level mixed-phase clouds over the Greenland and Norwegian seas. *Atmospheric Chemistry and Physics*, *17*(20), 12845–12869. https://doi.org/10.5194/acp-17-12845-2017

Mitchell, D. L. (1996). Use of mass-and area-dimensional power laws for determining precipitation particle terminal velocities. *Journal of the Atmospheric Sciences*, *53*(12), 1710–1723. https://doi.org/10.1175/1520-0469(1996)053<1710:uomaad>2.0.co;2

Mori, T., Kondo, Y., Ohata, S., Goto-Azuma, K., Fukuda, K., Ogawa-Tsukagawa, Y., et al. (2021). Seasonal variation of wet deposition of black carbon at Ny-Ålesund, Svalbard. *Journal of Geophysical Research: Atmospheres*, *126*, e2020JD034110. https://doi.org/10.1029/2020JD034110

Morrison, H., de Boer, G., Feingold, G., Harrington, J., Shupe, M. D., & Sulia, K. (2012). Resilience of persistent Arctic mixed-phase clouds. *Nature Geoscience*, *5*(1), 11–17. https://doi.org/10.1038/ngeo1332

Myagkov, A., Kneifel, S., & Rose, T. (2020). Evaluation of the reflectivity calibration of W-band radars based on observations in rain. *Atmospheric Measurement Techniques*, *13*(11), 5799–5825. https://doi.org/10.5194/amt-13-5799-2020

Nomokonova, T., Ebell, K., Löhnert, U., Maturilli, M., & Ritter, C. (2020). The influence of water vapor anomalies on clouds and their radiative effect at Ny-Ålesund. *Atmospheric Chemistry and Physics*, *20*(8), 5157–5173. https://doi.org/10.5194/acp-20-5157-2020

Nomokonova, T., Ebell, K., Löhnert, U., Maturilli, M., Ritter, C., & O'Connor, E. (2019). Statistics on clouds and their relation to thermodynamic conditions at Ny-Ålesund using ground-based sensor synergy. *Atmospheric Chemistry and Physics*, *19*(6), 4105–4126. https://doi.org/10.5194/acp-19-4105-2019

Nomokonova, T., Ritter, C., & Ebell, K. (2019). HATPRO microwave radiometer measurements at AWIPEV, Ny-Ålesund (2016-2018). [Dataset]. PANGAEA. https://doi.pangaea.de/10.1594/PANGAEA.902183

Norgren, M. S., Boer, G. D., & Shupe, M. D. (2018). Observed aerosol suppression of cloud ice in low-level Arctic mixed-phase clouds. *Atmospheric Chemistry and Physics*, *18*(18), 13345–13361. https://doi.org/10.5194/acp-18-13345-2018

Ori, D., Schemann, V., Karrer, M., Dias Neto, J., von Terzi, L., Seifert, A., & Kneifel, S. (2020). Evaluation of ice particle growth in ICON using statistics of multi-frequency Doppler cloud radar observations. *Quarterly Journal of the Royal Meteorological Society*, *146*(733), 3830–3849. https://doi.org/10.1002/qj.3875

Ori, D., von Terzi, L., Karrer, M., & Kneifel, S. (2021). snowScatt 1.0: Consistent model of microphysical and scattering properties of rimed and unrimed snowflakes based on the self-similar Rayleigh-Gans Approximation. *Geoscientific Model Development*, *14*(3), 1511–1531. https://doi.org/10.5194/gmd-14-1511-2021

Oue, M., Kollias, P., Matrosov, S. Y., Battaglia, A., & Ryzhkov, A. V. (2021). Analysis of the microphysical properties of snowfall using scanning polarimetric and vertically pointing multi-frequency Doppler radars. *Atmospheric Measurement Techniques*, *14*(7), 4893–4913. Retrieved from https://amt.copernicus.org/articles/14/4893/2021/

Pfitzenmaier, L., Dufournet, Y., Unal, C. M., & Russchenberg, H. W. (2017). Retrieving fall streaks within cloud systems using Doppler radar. *Journal of Atmospheric and Oceanic Technology*, *34*(4), 905–920. https://doi.org/10.1175/JTECH-D-16-0117.1

Pfitzenmaier, L., Unal, C. M., Dufournet, Y., & Russchenberg, H. W. (2018). Observing ice particle growth along fall streaks in mixed-phase clouds using spectral polarimetric radar data. *Atmospheric Chemistry and Physics*, *18*(11), 7843–7862. https://doi.org/10.5194/acp-18-7843-2018

Proske, U., Ferrachat, S., Neubauer, D., Staab, M., & Lohmann, U. (2021). Assessing the potential for simplification in global climate model cloud microphysics. *Atmospheric Chemistry and Physics Discussions*, *22*, 4737–4762. https://doi.org/10.5194/acp-2021-801

Pruppacher, H. R., & Klett, J. D. (2012). *Microphysics of clouds and precipitation: Reprinted 1980*. Springer. https://doi.org/10.1007/978-94-009-9905-3

Rangno, A. L., & Hobbs, P. V. (2001). Ice particles in stratiform clouds in the Arctic and possible mechanisms for the production of high ice concentrations. *Journal of Geophysical Research: Atmospheres*, *106*(D14), 15065–15075. https://doi.org/10.1029/2000JD900286

Rose, T., Crewell, S., Löhnert, U., & Simmer, C. (2005). A network suitable microwave radiometer for operational monitoring of the cloudy atmosphere. *Atmospheric Research*, *75*(3), 183–200. https://doi.org/10.1016/j.atmosres.2004.12.005

Ruiz-Donoso, E., Ehrlich, A., Schäfer, M., Jäkel, E., Schemann, V., Crewell, S., et al. (2020). Small-scale structure of thermodynamic phase in Arctic mixed-phase clouds observed by airborne remote sensing during a cold air outbreak and a warm air advection event. *Atmospheric Chemistry and Physics*, *20*(9), 5487–5511. https://doi.org/10.5194/acp-20-5487-2020

Scarchilli, C., Ciardini, V., Grigioni, P., Iaccarino, A., De Silvestri, L., Proposito, M., et al. (2020). Characterization of snowfall estimated by in situ and ground-based remote-sensing observations at Terra Nova Bay, Victoria Land, Antarctica. *Journal of Glaciology*, *66*(260), 1006–1023. https://doi.org/10.1017/jog.2020.70

Schäfer, M., Loewe, K., Ehrlich, A., Hoose, C., & Wendisch, M. (2018). Simulated and observed horizontal inhomogeneities of optical thickness of Arctic stratus. *Atmospheric Chemistry and Physics*, *18*(17), 13115–13133. https://doi.org/10.5194/acp-18-13115-2018

Serreze, M. C., & Barry, R. G. (2011). Processes and impacts of arctic amplification: A research synthesis. *Global and Planetary Change*, *77*(1–2), 85–96. https://doi.org/10.1016/j.gloplacha.2011.03.004

Shupe, M. D. (2011). Clouds at Arctic atmospheric observatories. Part II: Thermodynamic phase characteristics. *Journal of Applied Meteorology and Climatology*, *50*(3), 645–661. https://doi.org/10.1175/2010jamc2468.1

Shupe, M. D., & Intrieri, J. M. (2004). Cloud radiative forcing of the Arctic surface: The influence of cloud properties, surface albedo, and solar zenith angle. *Journal of Climate*, *17*(3), 616–628. https://doi.org/10.1175/1520-0442(2004)017<0616:crfota>2.0.co;2

Shupe, M. D., Kollias, P., Persson, P. O. G., & McFarquhar, G. M. (2008). Vertical motions in Arctic mixed-phase stratiform clouds. *Journal of the Atmospheric Sciences*, *65*(4), 1304–1322. https://doi.org/10.1175/2007JAS2479.1

Shupe, M. D., Matrosov, S. Y., & Uttal, T. (2006). Arctic mixed-phase cloud properties derived from surface-based sensors at SHEBA. *Journal of the Atmospheric Sciences*, *63*(2), 697–711. https://doi.org/10.1175/JAS3659.1

Silber, I., McGlynn, P. S., Harrington, J. Y., & Verlinde, J. (2021). Habit-dependent vapor growth modulates Arctic supercooled water occurrence. *Geophysical Research Letters*, *48*(10), e2021GL092767. https://doi.org/10.1029/2021GL092767

Simpfendoerfer, L. F., Verlinde, J., Harrington, J. Y., Shupe, M. D., Chen, Y.-S., Clothiaux, E. E., & Golaz, J.-C. (2019). Formation of Arctic stratocumuli through atmospheric radiative cooling. *Journal of Geophysical Research: Atmospheres*, *124*(16), 9644–9664. https://doi.org/10.1029/2018JD030189

Slater, B., & Michaelides, A. (2019). Surface premelting of water ice. *Nature Reviews Chemistry*, *3*(3), 172–188. https://doi.org/10.1038/s41570-019-0080-8

Solomon, A., Boer, G. d., Creamean, J. M., McComiskey, A., Shupe, M. D., Maahn, M., & Cox, C. (2018). The relative impact of cloud condensation nuclei and ice nucleating particle concentrations on phase partitioning in Arctic mixed-phase stratocumulus clouds. *Atmospheric Chemistry and Physics*, *18*(23), 17047–17059. https://doi.org/10.5194/acp-18-17047-2018

Solomon, A., Feingold, G., & Shupe, M. D. (2015). The role of ice nuclei recycling in the maintenance of cloud ice in Arctic mixed-phase stratocumulus. *Atmospheric Chemistry and Physics*, *15*(18), 10631–10643. Retrieved from https://acp.copernicus.org/articles/15/10631/2015/

Solomon, A., Shupe, M. D., Persson, O., Morrison, H., Yamaguchi, T., Caldwell, P. M., & de Boer, G. (2014). The sensitivity of springtime Arctic mixed-phase stratocumulus clouds to surface-layer and cloud-top inversion-layer moisture sources. *Journal of the Atmospheric Sciences*, *71*(2), 574–595. https://doi.org/10.1175/jas-d-13-0179.1

Solomon, A., Shupe, M. D., Persson, P. O. G., & Morrison, H. (2011). Moisture and dynamical interactions maintaining decoupled Arctic mixed-phase stratocumulus in the presence of a humidity inversion. *Atmospheric Chemistry and Physics*, *11*(19), 10127–10148. https://doi.org/10.5194/acp-11-10127-2011

Sotiropoulou, G., Sedlar, J., Tjernström, M., Shupe, M. D., Brooks, I. M., & Persson, P. O. G. (2014). The thermodynamic structure of summer Arctic stratocumulus and the dynamic coupling to the surface. *Atmospheric Chemistry and Physics*, *14*(22), 12573–12592. https://doi.org/10.5194/acp-14-12573-2014

Souverijns, N., Gossart, A., Lhermitte, S., Gorodetskaya, I. V., Grazioli, J., Berne, A., et al. (2018). Evaluation of the CloudSat surface snowfall product over Antarctica using ground-based precipitation radars. *The Cryosphere*, *12*(12), 3775–3789. https://doi.org/10.5194/tc-12-3775-2018

Szyrmer, W., & Zawadzki, I. (2014). Snow studies. Part IV: Ensemble retrieval of snow microphysics from dual-wavelength vertically pointing radars. *Journal of the Atmospheric Sciences*, *71*(3), 1171–1186. https://doi.org/10.1175/JAS-D-12-0286.1

Takahashi, T. (2014). Influence of liquid water content and temperature on the form and growth of branched planar snow crystals in a cloud. *Journal of the Atmospheric Sciences*, *71*(11), 4127–4142. https://doi.org/10.1175/JAS-D-14-0043.1

Takahashi, T., Endoh, T., Wakahama, G., & Fukuta, N. (1991). Vapor diffusional growth of free-falling snow crystals between −3 and −23°C. *Journal of the Meteorological Society of Japan Series II*, *69*(1), 15–30. https://doi.org/10.2151/jmsj1965.69.1_15

Tan, I., & Storelvmo, T. (2019). Evidence of strong contributions from mixed-phase clouds to Arctic climate change. *Geophysical Research Letters*, *46*(5), 2894–2902. https://doi.org/10.1029/2018GL081871

Thurai, M., Huang, G. J., Bringi, V. N., Randeu, W. L., & Schönhuber, M. (2007). Drop shapes, model comparisons, and calculations of polarimetric radar parameters in rain. *Journal of Atmospheric and Oceanic Technology*, *24*(6), 1019–1032. https://doi.org/10.1175/JTECH2051.1

Tridon, F., & Battaglia, A. (2015). Dual-frequency radar Doppler spectral retrieval of rain drop size distributions and entangled dynamics variables. *Journal of Geophysical Research: Atmospheres*, *120*(11), 5585–5601. https://doi.org/10.1002/2014JD023023

Tridon, F., Battaglia, A., Chase, R. J., Turk, F. J., Leinonen, J., Kneifel, S., et al. (2019). The microphysics of stratiform precipitation during OLYMPEX: Compatibility between triple-frequency radar and airborne in situ observations. *Journal of Geophysical Research: Atmospheres*, *124*(15), 8764–8792. https://doi.org/10.1029/2018JD029858

Tridon, F., Battaglia, A., & Kneifel, S. (2020). Estimating total attenuation using Rayleigh targets at cloud top: Applications in multilayer and mixed-phase clouds observed by ground-based multifrequency radars. *Atmospheric Measurement Techniques*, *13*(9), 5065–5085. https://doi.org/10.5194/amt-13-5065-2020

Vassel, M., Ickes, L., Maturilli, M., & Hoose, C. (2019). Classification of Arctic multilayer clouds using radiosonde and radar data in Svalbard. *Atmospheric Chemistry and Physics*, *19*(7), 5111–5126. https://doi.org/10.5194/acp-19-5111-2019

Waterman, P. (1965). Matrix formulation of electromagnetic scattering. *Proceedings of the IEEE*, *53*(8), 805–812. https://doi.org/10.1109/PROC.1965.4058

Wendisch, M., Macke, A., Ehrlich, A., Lüpkes, C., Mech, M., Chechin, D., et al. (2019). The Arctic cloud puzzle: Using ACLOUD/PASCAL multiplatform observations to unravel the role of clouds and aerosol particles in arctic amplification. *Bulletin of the American Meteorological Society*, *100*(5), 841–871. https://doi.org/10.1175/BAMS-D-18-0072.1

Westbrook, C. D., Hogan, R. J., & Illingworth, A. J. (2008). The capacitance of pristine ice crystals and aggregate snowflakes. *Journal of the Atmospheric Sciences*, *65*(1), 206–219. https://doi.org/10.1175/2007jas2315.1

Williams, C. R., Gage, K. S., Clark, W., & Kucera, P. (2005). Monitoring the reflectivity calibration of a scanning radar using a profiling radar and a disdrometer. *Journal of Atmospheric and Oceanic Technology*, *22*(7), 1004–1018. https://doi.org/10.1175/JTECH1759.1

Young, G., Jones, H. M., Choularton, T. W., Crosier, J., Bower, K. N., Gallagher, M. W., et al. (2016). Observed microphysical changes in Arctic mixed-phase clouds when transitioning from sea ice to open ocean. *Atmospheric Chemistry and Physics*, *16*(21), 13945–13967. https://doi.org/10.5194/acp-16-13945-2016

Yuter, S. E., & Houze, R. A., Jr. (1995). Three-dimensional kinematic and microphysical evolution of Florida cumulonimbus. Part II: Frequency distributions of vertical velocity, reflectivity, and differential reflectivity. *Monthly Weather Review*, *123*(7), 1941–1963. https://doi.org/10.1175/1520-0493(1995)123<1941:tdkame>2.0.co;2

Zängl, G., Reinert, D., Rípodas, P., & Baldauf, M. (2015). The ICON (ICOsahedral Non-hydrostatic) modelling framework of DWD and MPI-M: Description of the non-hydrostatic dynamical core. *Quarterly Journal of the Royal Meteorological Society*, *141*(687), 563–579. https://doi.org/10.1002/qj.2378

Zhang, D., Wang, Z., Luo, T., Yin, Y., & Flynn, C. (2017). The occurrence of ice production in slightly supercooled Arctic stratiform clouds as observed by ground-based remote sensors at the ARM NSA site. *Journal of Geophysical Research: Atmospheres*, *122*(5), 2867–2877. https://doi.org/10.1002/2016JD026226

Zhao, M., & Wang, Z. (2010). Comparison of arctic clouds between European Center for Medium-Range Weather Forecasts Simulations and Atmospheric Radiation Measurement Climate Research Facility long-term observations at the North Slope of Alaska Barrow site. *Journal of Geophysical Research: Atmospheres*, *115*(D23), D23202. https://doi.org/10.1029/2010JD014285

Zuidema, P., Baker, B., Han, Y., Intrieri, J., Key, J., Lawson, P., et al. (2005). An Arctic springtime mixed-phase cloudy boundary layer observed during SHEBA. *Journal of the Atmospheric Sciences*, *62*(1), 160–176. https://doi.org/10.1175/JAS-3368.1